Mass transfer at the ocean-atmosphere interface: the role of wave breaking, droplets and bubbles.

Luc Deike,[1,2]

[1]Department of Mechanical and Aerospace Engineering, Princeton University, Princeton, New Jersey, 08544, United States; email: ldeike@princeton.edu
[2]High Meadows Environmental Institute, Princeton University, Princeton, NJ 08544, USA

Keywords

air-sea interaction, wave breaking, bubbles, gas transfer, sea spray, turbulence.

Abstract

Breaking waves modulate the transfer of energy, momentum and mass between the ocean and atmosphere, controlling processes critical to the climate system, from gas exchange of carbon dioxide and oxygen, to the generation of sea spray aerosols which can be transported in the atmosphere and serve as cloud condensation nuclei. An outsized role is played by the smallest components: drops and bubbles generated by breaking waves. This fascinating problem is characterized by a wide range of scales, from wind forcing the wave field at scales of O(1km-1m), to the dynamics of wave breaking, O(10-1m), to air bubble entrainment, dynamics and dissolution in the water column O(1m-10μm), to bubble bursting, O(10mm to 1μm) generating sea spray droplets O(0.5mm to 0.5μm) ejected into the atmospheric turbulent boundary layers. I will discuss recent progress to bridge these scales, identifying the controlling processes, and proposing a path toward mechanistic parameterizations of air-sea mass exchange, naturally accounting for sea-state effects.

1. Introduction

Physical processes at the ocean-atmosphere interface have a large effect on climate and weather by controlling the transfer of momentum, energy and mass. Without wave breaking, transport between the ocean and the atmosphere is through slow conduction and molecular diffusion, while wave breaking is a transitional process from laminar to turbulent flow. When waves are breaking, the surface experiences dramatic changes, with sea spray ejection in the atmosphere and air entrainment into the ocean water. The dynamics and statistics of wave breaking in a particular ocean location depends mainly on the local wave state not the wind velocity, while current parameterizations for air-sea interactions in oceanic and atmospheric models remain based exclusively on the wind speed.

The processes associated with surface ocean breaking waves span multiple fields of ocean and atmospheric sciences, as breaking waves regulates ocean-atmosphere interaction from local to global scales. Breaking limits the height of ocean waves, transfers momentum from waves to current and modulates upper ocean turbulence (Melville 1996; Sullivan & McWilliams 2010; Cavaleri et al. 2012; Perlin et al. 2013). In the present review, I will focus on the role of wave breaking and the associated bubbles entrained in water and drops ejected in the atmosphere in controlling mass exchange. Air bubbles entrained by breaking contribute to gas exchange, with approximately 30% of the CO_2 released into the atmosphere taken up by the ocean. Recent reviews by Wanninkhof et al. (2009); Garbe et al. (2014); Woolf et al. (2019) have discussed air-sea gas exchange, and highlighted the remaining uncertainties in quantifying the role of air bubbles entrained by wave breaking in the transfer of gases critical to the climate system. Breaking is responsible for sea spray formation, through direct atomization, and while small bubbles may be dissolved into the water column, larger bubbles entrained by breaking rise back to the surface and collapse. This generates spray, which is transported into the atmosphere and ultimately evaporates leaving water vapour, important for the thermodynamics of the atmosphere, and salt crystals that affect the radiative balance of the atmosphere and form cloud condensation nuclei, which has been reviewed by Lewis & Schwartz (2004); de Leeuw et al. (2011); Veron (2015). The implications of organic and sea salt aerosols on atmospheric chemistry are reviewed in Quinn et al. (2015); Cochran et al. (2017); Bertram et al. (2018) and highlight the importance in understanding the sea spray droplet production processes.

These numerous studies highlight the uncertainties in bubble mediated gas exchange and sea spray production, represented in large scale models by the *gas transfer velocity* and the *sea spray generation function*. These functions control the associated fluxes of gases, moisture and sea salt, key to the climate system, and are usually only parameterized as a function of wind speed, while local processes are more tightly controlled by the sea state.

The uncertainties for both the bubble mediated gas transfer and sea spray aerosol production by bubble bursting come in part from the large range of scales, summarized in figure 1, ranging from bubbles O(μm to mm) to breaking waves O(1-10m) to large scale wave patterns O(100m-1km) and wind forcing; in part from the difficulty in field measurements (especially at high wind speed) and finally the lack of connections between the idealized mechanistic descriptions of the individual processes and the ocean conditions. Above a certain wind speed, typically 7 m/s, waves start to break, entraining air bubbles visible through whitecaps at the ocean surface. The breaking fronts $\Lambda(c)$ moving at a certain speed c are illustrated in fig. 1a, following the representation introduced by Phillips (1985), which will be used to relate the breaking distribution to the air-sea fluxes associated with the entrained bubbles. The speed of the breaking fronts in the field is typically from 1 to

$\Lambda(c)dc$: is the averaged length of breaking crest moving at speed c, and characterize the breaking statistics

10m/s. A single breaking event is illustrated in fig. 1b, characterized by its height O(1-10m) at breaking h, which together with c will control turbulence generation and bubble plume entrainment. The bubbles, O(μm to mm), entrained by breaking will evolve in the upper ocean turbulent flow, exchanging gas, and might rise to the surface where they will burst and produce film and jet drops (fig. 1c,d,e).

Bridging the scales involved in mass exchange between the ocean and the atmosphere has been a longstanding issue, the associated uncertainties in the production processes propagating into uncertainties in large scale modeling, and will be the focus of this review. §2 presents the dynamics of wave breaking, focusing on the properties of the post-breaking two-phase turbulent flow, based on canonical experiments and simulations. §3 presents the ocean wave scales, focusing on statistical representations of the waves and wave breaking. This is combined with our understanding of the breaking dynamics to obtain a multi-scale description of energy dissipation and air entrainment by breaking waves, which can then be used to estimate mass fluxes controlled by breaking waves at the ocean-atmosphere interface. I describe two important applications of this framework: gas exchange (§4) and sea spray production by bubble bursting (§5), yielding sea-state formulations for the gas transfer velocity and sea spray generation function.

The scope is wide, and each of these processes would deserve its own review, and I offer here sincere apologies to those whose work on mass exchange at the air-sea interface I have overlooked, whether as a result of editorial constraints or by my own omission. I will focus on providing a consistent framework to bridge the scales, presenting scaling models derived from mechanistic studies at the bubble, droplet and breaking wave scales combined with a statistical representation of the sea-state. I will show how this strategy can provide sea-state dependent formulations for ocean-atmosphere fluxes, focusing on bubble mediated gas transfer and sea spray production by bubble bursting.

2. Wave breaking dynamics: energetics and air bubbles entrainment

2.1. Energy dissipation by a breaking wave and the scales of breaking

2.1.1. Canonical breaking waves in the laboratory and in direct numerical simulations. The importance and complexity of deep ocean breaking waves, combined with the difficulties in measuring and observing a two-phase turbulent process at sea has driven experimental, numerical and theoretical work, aiming to elucidate the physics of breaking waves.

Numerous studies have investigated the routes leading to breaking, including linear, nonlinear focusing and modulation instability. The quest for an universal breaking criterion remains an outstanding challenge, while the definition of a breaking event in itself is non-trivial, from early interface disturbance, to micro-breaking, to parasitic capillaries and to air entrainment (Melville 1982; Rapp & Melville 1990; Duncan 2001; Perlin et al. 2013; Banner & Peirson 2007; Saket et al. 2017).

Here, I will focus on post-breaking properties, and characterize the transition from a laminar wave flow to a two-phase turbulent flow (Duncan 1981; Rapp & Melville 1990; Lamarre & Melville 1991). Laboratory experiments using the linear focusing method have allowed to generate highly reproducible breaking packets, illustrated in figure 2, which combined with progress in two-phase flow measurement techniques led to high quality data of energy dissipation, turbulence and current generation (Rapp & Melville 1990; Melville et al. 2002; Banner & Peirson 2007; Tian et al. 2010; Drazen et al. 2008). The main controlling variables of the post-breaking flow are identified as the breaker speed c, and

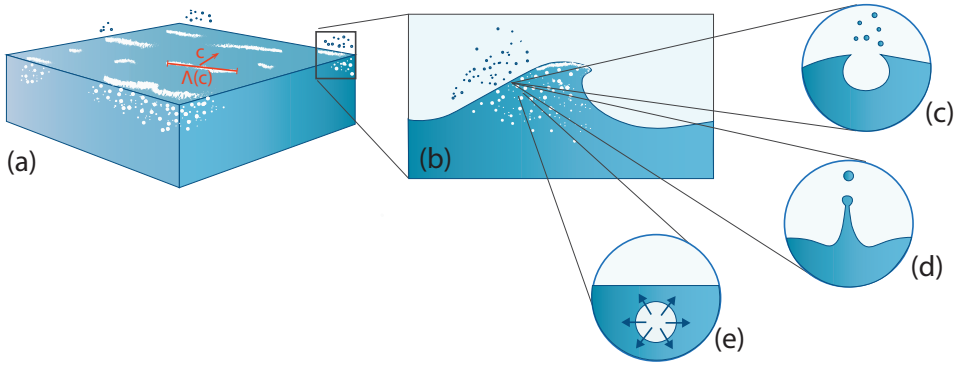

Figure 1

Sketch of the multi-scale approach discussed in this review to model mass exchange due to breaking waves, drops and bubbles. At moderate to high wind speeds, breaking waves form whitecaps on the ocean surface. The breaking statistics can be described by the distribution of length of breaking crest, $\Lambda(c)$, moving at speed c, typically from 1 to 20 m/s. Each breaker dynamics is assumed self-similar and is described by its speed c and slope S, leading to scaling models for the associated energy dissipation, air entrainment and bubble statistics. At the smallest scales, bubbles of sizes R_b from O(1μm) to O(10mm) are exchanging gas in the turbulent upper ocean, and bursting at the surface to produce liquid sea spray, through film and jet drops, of sizes r_d from O(0.1μm) to O(1mm).

wave slope $S = hk$, where h is the breaking height and k the characteristic wavenumber.

Separately, numerical simulations have brought insight into the breaking dynamics, starting with non-linear free surface potential solvers resolving up to the breaking point (Longuet-Higgins & Dommermuth 1997; Dommermuth et al. 1988), as well as spilling breakers, and micro-breakers or parasitic capillary waves (Melville & Fedorov 2015; Tsai & Hung 2007). More recently, direct numerical simulations (DNS) of the two-phase Navier-Stokes equations have started to become available to capture post-breaking properties, in two-dimensions (Chen et al. 1999; Iafrati 2009; Deike et al. 2015) and finally in three dimensions (Deike et al. 2016; Wang et al. 2016; Yang et al. 2018; Chan et al. 2020; Mostert et al. 2021). These DNS usually consider compact wave trains at moderate Reynolds number, and have demonstrated their ability to reproduce energy dissipation and other post-breaking features from laboratory experiments, and explored the resulting two-phase turbulent flow. Together with DNS, large eddy simulations (LES) help fill the gap between the DNS and the laboratory scales (Lubin & Glockner 2015; Derakhti & Kirby 2016).

2.1.2. The inertial scaling for energy dissipation by breaking waves. Duncan (1981); Phillips (1985) described the dissipation rate due to breaking, per unit length of breaking crest, ϵ_l, assuming that the breaking zone extends down the forward face of the wave over a fixed fraction of its amplitude and that its shape is geometrically similar for waves of different scales, so that,

$$\epsilon_l = b\rho c^5/g, \tag{1}$$

where g is gravity, ρ the water density. This introduces the non-dimensional breaking parameter, b, first assumed to be a non-dimensional constant, but shown to vary over

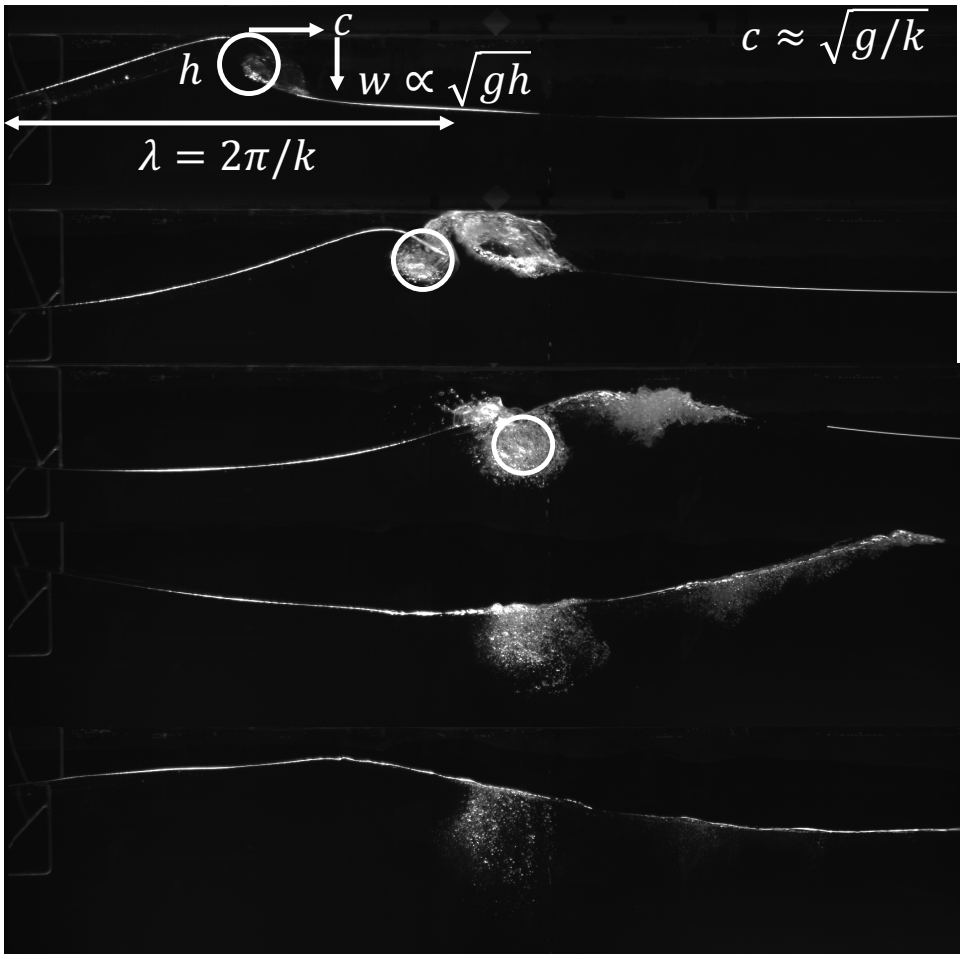

Figure 2

Breaking sequence in the laboratory indicating the breaking scales, the breaker crest speed c, height h, wavelength λ, the jet ballistic velocity $w \sim \sqrt{gh}$, and resulting bubbly turbulent cloud, with a life-time τ_b. The sequence shows steepening and jet formation, impact at speed w, creation of a turbulent bubbly cloud of cross section $A \propto h^2$, plume evolution with bubble break-up, rising back at the surface and bursting over τ_b.

several orders of magnitude by extensive experimental scrutiny (Duncan 1981; Rapp & Melville 1990; Drazen et al. 2008; Tian et al. 2010), when varying the breaking wave slope $S = hk$.

Drazen et al. (2008) proposed that the breaking strength and resulting turbulence is controlled by the local breaking height, together with the breaker speed. The total dissipation rate per unit breaking crest length, ϵ_l can be related to the local turbulent dissipation rate ε considering that the turbulence is confined to a volume $\mathcal{V} = AL_c$, of cross section $A \simeq \pi h^2/4$ (Drazen et al. 2008), and L_c the length of breaking crest, so that $\epsilon_l = \rho A \varepsilon$. The local turbulent dissipation rate after impact is described by a turbulent inertial scaling, and

links the local turbulence dissipation rate to the integral length scale, $\sim h$, and breaking intensity quantified by the ballistic velocity of the falling jet, $w \sim \sqrt{gh}$ (Drazen et al. 2008; Erinin et al. 2019). The local turbulence dissipation rate then reads

$$\varepsilon \propto \sqrt{gh}^3/h, \tag{2}$$

so that the dissipation rate per unit length of breaking crest, $\epsilon_l = \rho A \varepsilon = \chi S^{5/2} \rho c^5/g$, with χ an $O(1)$ constant and $b = \chi S^{5/2}$; the breaking parameter is now a function of the breaking slope. This local scaling has been extensively tested and related to the initial conditions of the breaking packet (slope, bandwidth, and speed) using laboratory experiments (Duncan 1981; Rapp & Melville 1990; Banner & Peirson 2007; Drazen et al. 2008; Grare et al. 2013) and numerical simulations (Iafrati 2009; Deike et al. 2015, 2016; Derakhti & Kirby 2016; De Vita et al. 2018). Figure 3a shows b as a function of the slope S, with the data very well described by the semi-empirical scaling accounting for a breaking threshold defined by a critical slope S_0 (Romero et al. 2012),

b: is the breaking parameter, is a non-dimensional measure of the energy dissipation and is mainly a function of breaker speed and slope.

$$b = \chi_T (S - S_0)^{5/2}, \tag{3}$$

where $\chi_T = 0.4$ and $S_0 = 0.08$ adjusted to the data.

We note that the breaking speed has been observed to move at a velocity c_b slightly below the phase velocity, $0.8c \leq c_b \leq c$ (Rapp & Melville 1990; Banner & Peirson 2007; Saket et al. 2017). This has motivated discussions on the definition of the slope, either from upstream conditions, or closer to the breaking point which impacts the coefficients χ_T and S_0. This underlines the fact that a critical slope is an imperfect breaking criteria, with scatter between various experiments and types of breakers, and has prompted extensive work on kinematic thresholds (Perlin et al. 2013; Saket et al. 2017; Derakhti et al. 2020).

Nevertheless, this formulation for the breaking parameter and energy dissipation provides constraints on the wave breaking energy budget, and in the following, we will consider that the breaking speed c and the wavenumber k can be related to the dispersion relation of ocean gravity waves in deep water, $c = \sqrt{g/k}$. Note that scaling arguments, using the breaking height and speed as the controlling scales, have been proposed to describe the generation of vorticity (Pizzo & Melville 2013), current (Pizzo et al. 2016), and surface drift induced by breaking (Deike et al. 2017b; Pizzo et al. 2019).

2.2. Air entrainment and bubble distribution under a breaking wave

Together with total air entrainment, the shape of the bubble size distribution is the most important characteristic of the bubble formation process as it will control mass exchange. Lamarre & Melville (1991); Duncan (1981); Blenkinsopp & Chaplin (2010); Deike et al. (2016); Mostert et al. (2021) showed that the breaker geometry constrains the maximum volume of air entrained and that the air cavity cross section scales as $A \propto h^2$, with entrainment of a relatively homogeneous bubble cloud up to a depth h (see fig. 2).

Garrett et al. (2000) proposed a *steady* model of a turbulent break-up cascade for the bubble size distribution (per unit volume) $N(R_b)$, R_b the bubble radius, assuming a *constant* air flow rate per unit volume of water Q, $N(r) \propto Q$, and the process to be controlled only by the local (time-averaged) turbulent dissipation rate ε, so that dimensional analysis yields

$$N(R_b) \propto Q \varepsilon^{-1/3} R_b^{-10/3}. \tag{4}$$

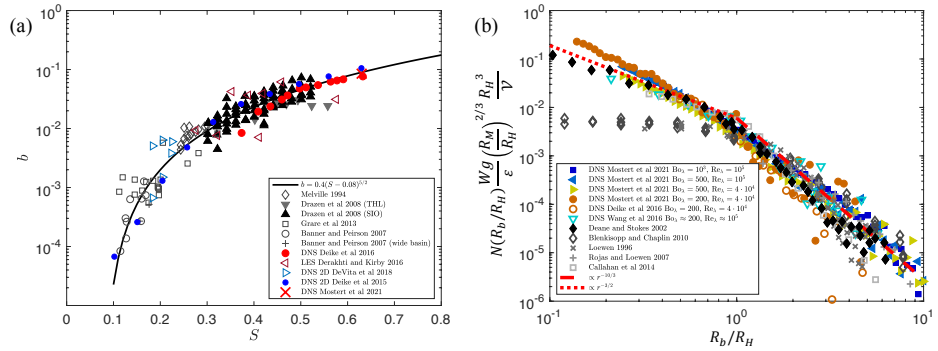

Figure 3

Energy dissipation and bubble size distribution from laboratory experiments and numerical simulations of canonical breaking waves. Black and grey symbols are experimental data; while colored symbols are numerical work. (a) Breaking parameter b as a function of the initial wave slope S, for DNS, LES and laboratory experiments. The solid line is the semi-empirical formulation based on the inertial argument, Eq. 3, $b = 0.4(S - 0.08)^{5/2}$ (Romero et al. 2012). All data are very well captured by the solid line given the complexity of the process and the differences in initiating breaking. (b) Bubble size distributions, as a function of R_b/R_H, over the active breaking time, normalized following eq. 6 (Deike et al. 2016; Mostert et al. 2021) for their data and for the experimental data from Deane & Stokes (2002) (other data are arbitrary scaled vertically since not enough information is provided). Data collapse onto a single curve, for the super-Hinze regime, $R_b^{-10/3}$ and sub-Hinze regime $R_b^{-3/2}$ (for most data).

This result can also be understood by a population balance argument, with the break-up cascade local in scale, and the break-up time driven by the turbulence at the scale of the bubble, $\tau_c \propto \varepsilon^{-1/3} R_b^{2/3}$, which yields $N(R_b) \propto R_b^{-10/3}$. Several experimental studies (Loewen et al. 1996; Deane & Stokes 2002; Rojas & Loewen 2007; Blenkinsopp & Chaplin 2010) have confirmed this scaling, together with recent DNS of breaking waves (Wang et al. 2016; Deike et al. 2016; Chan et al. 2020; Mostert et al. 2021) (fig. 3). The turbulent break-up cascade was also characterized by DNS of single large bubbles or droplets breaking in an homogeneous and isotropic turbulent flow (Soligo et al. 2019; Rivière et al. 2021).

The Hinze scale R_H: compares the action of surface tension and turbulence and corresponds to the critical size below which bubbles do not break under the water turbulence.

The local turbulent break-up cascade assumes an inertial subrange and a *direct cascade* process: air is injected at large scales (large bubbles) by the entrainment process and turbulent fluctuations break them into smaller bubbles. The cascade process ends at the scale where surface tension prevents further bubble break-up, the Hinze scale (Hinze 1955):

$$R_H = \mathcal{C}(\gamma/\rho)^{3/5} \varepsilon^{-2/5}, \tag{5}$$

where $\mathcal{C}$ is a dimensionless constant O(1) (Martinez-Bazan et al. 1999; Perrard et al. 2021; Rivière et al. 2021). Under typical breaking conditions, $R_H \approx 1 - 2$mm, and about 95% of the entrained air volume is contained in the super-Hinze ($R_b > R_H$) bubbles (Deane & Stokes 2002; Mostert et al. 2021).

The statistics of bubbles below the Hinze scale has been reported by Deane & Stokes (2002), as $N(R_b) \propto R_b^{-3/2}$, while other experimental measurements have shown a large scatter as illustrated in fig. 3. Recent DNS of breaking waves and bubble break-up have provided further evidence for the $N(R_b) \propto R_b^{-3/2}$ regime (Rivière et al. 2021; Mostert et al.

The bubble size distribution under a breaking wave $N(R_b)$: is separated into two regimes: for $R_b > R_H$, a turbulent break-up cascade is observed, $N(R_b) \propto R_b^{-10/3}$, and contains about 95% of the initial entrained volume. For $R_b < R_H$ most data follow $N(R_b) \propto R_b^{-3/2}$.

2021), with production due to the fragmentation of highly deformed large super-Hinze bubbles, yielding a non-local cascade (Rivière et al. 2021), as well as through entrainment at impact (Chan et al. 2020; Mostert et al. 2021).

Deike et al. (2016); Mostert et al. (2021) combine the geometrical constraint of the entrained bubble cloud with an energy balance between buoyancy forces and turbulent dissipation, to propose a relationship describing the time evolution of the air entrained by the bubble plume with the turbulence dissipation rate. Integrating over the breaking time, or bubble plume time τ_b, and considering R_M the entrained cavity size as the injection size, so that $AL_c \equiv \mathcal{V} \propto R_M^2 L_c$, the size distribution reads,

$$N(R_b/R_H) = \frac{B}{2\pi}\frac{\varepsilon}{Wg}\left(\frac{R_b}{R_H}\right)^{-10/3}\frac{\mathcal{V}}{R_H^3}\left(\frac{R_M}{R_H}\right)^{-2/3}. \tag{6}$$

Here, W is a characteristic plume velocity, related to the breaking height and plume lifetime, $\tau_b W \propto h$ (Callaghan et al. 2013; Lamarre & Melville 1991; Deike et al. 2016, 2017a), and $B \approx 0.1$ a non-dimensional constant, related to the ratio between the total dissipation rate and the contribution to air entrainment. The sub-Hinze scale regime is obtained by continuity. As shown in figure 3b, this model describes very well the experimental and numerical data available (with some scatter remaining in the sub-Hinze regime). The total volume of entrained air during the breaking process is obtained by integration, and assuming separation of scales $R_H \ll R_M$,

$$V = \int_{R_H}^{R_M}(4\pi/R_b)R_b^3 N(R_b)dR_b = Bb\frac{L_c c^5}{Wg^2}. \tag{7}$$

Equation 7 provides a constraint on air-entrainment based on the breaking wave characteristic scales, namely its speed c and slope S (since $b \propto S^{5/2}$).

3. Ocean waves: wave breaking statistics and dynamics.

We have discussed our understanding of canonical breaking waves in well controlled laboratory and numerical experiments, and introduced scaling laws for the energy dissipation and air bubble entrainment in the near surface turbulent layer. While uncertainties remain, these relationships serve as a basis to construct mechanistic models of air-sea fluxes, by assuming that each breaking wave in the field will behave similarly, and can be described by its local *breaking crest speed* and *slope*. We now characterize the statistics of waves and breaking waves, as a function of large scale wind forcing.

3.1. The wave spectrum

3.1.1. Source terms. The directional wave spectrum at the ocean surface $F(\mathbf{k})$, describes the wave energy density per scale, with $\langle \eta^2 \rangle = \int\int F(\mathbf{k})d\mathbf{k}$, the variance of the wave surface elevation. We recall some essential elements while extensive studies have been performed, see for example Komen et al. (1996). Locally the wave field is related to the action of wind, leading to wave growth as it inputs energy and momentum into the waves, as well as non-linear transfer through the scales (both forward and inverse cascade being possible for surface gravity waves) and dissipation, mainly by breaking. Each of these processes are in principle dynamically coupled. However, within a statistical description, the spectral evolution of the wave spectrum is obtained by solving the wave action equation, relating the

Lagrangian derivative of the spectral density following a wave packet at its group speed in both physical and spectral spaces to source terms able to input, output and transfer energy through the scales (Komen et al. 1996; Ardhuin et al. 2010):

$$\frac{dN(\mathbf{k})}{dt} = (S_{wind} + S_{diss} + S_{nl})/\omega, \tag{8}$$

where $N(\mathbf{k}) = F(\mathbf{k})/\omega$ is the wave action and $\omega = \sqrt{gk}$ the angular frequency of gravity waves in deep water. The wind forcing depends on the wind friction velocity u_* (defined through the wind stress at the ocean surface), with typical functional form, $S_{wind} \propto \frac{\rho_a}{\rho_w}(\frac{u_*}{c})^2 \omega F(\mathbf{k})$, and empirical formulation for the misalignement between waves and wind (Miles 1957; Plant 1982; Komen et al. 1996). The non-linear interaction term, S_{nl} transfers energy through the scales through a four-wave resonant process (Hasselmann 1962), while dissipation is mainly due to breaking waves (Phillips 1985).

u_*: is the wind friction velocity defined by the wind stress at the ocean surface $\tau = \rho_a u_*^2$ (ρ_a the air density), and characterize the wind forcing. It is related to the wind speed at 10 meters U_{10} through a drag coefficient.

3.1.2. Equilibrium and saturation ranges. For simplicity, we consider the omnidirectional (angle integrated) spectrum, $\phi(k) = \int F(k,\theta) k d\theta$ to discuss the spectrum shape. From the peak of the wave spectrum k_p, which can be related to wind forcing and fetch (the distance over which wind has been blowing without obstruction) through the so-called fetch limited relationships (Toba 1972; Hasselmann et al. 1973; Romero & Melville 2010), to a transition wave number k_n, the spectrum can be described as a balance between the three main source terms, which yields an *equilibrium range* (Toba 1972; Phillips 1985),

$$\phi(k) = \beta u_* g^{-1/2} k^{-5/2}, \text{ for } k_p < k < k_n. \tag{9}$$

The Toba constant, β, is determined empirically and has been described as a function of the wave age $\beta \approx 0.016(c_p/u_*)^{0.53}$ (Romero & Melville 2010). The corresponding frequency spectrum is $\phi(\omega) = \beta u_* g \omega^{-4}$ through $\phi(k)dk = \phi(\omega)d\omega$. Note that the equilibrium range is compatible with the independent description of weak-wave turbulence theory, which provides stationary solutions, assuming energy injection and dissipation to occur at very different scales and non-linear interaction to transfer energy from large to small scale, yielding a direct cascade $\phi(k) \propto P^{1/3} g^{-1/2} k^{-5/2}$, where P is a conserved wave energy flux (Zakharov et al. 2012). This result is dimensionally consistent with eq. 9, since $u_* \propto P^{1/3}$. In the weak-turbulence framework, an inverse cascade describes the frequency downshift due to wind forcing during the development of the wave spectrum from a calm sea to a fully developed spectrum, and yields formulations of the fetch limited relationships (Zakharov et al. 2015).

At higher frequency, above a transition wave-number k_n, Phillips (1985) describes the saturation spectrum, where breaking dominates the dynamics, with $k_n \approx (2\hat{B}/\beta)^2 g u_*^{-2}$, with $\hat{B}$ the saturation, which presents a wave age dependency (Romero & Melville 2010; Lenain & Melville 2017b; Lenain & Pizzo 2020). For $k > k_n$, the *saturation spectrum* follows

$$\phi(k) = \hat{B} k^{-3}, \text{ for } k > k_n. \tag{10}$$

This description of the wave spectrum has been recently well documented and validated through spatial and temporal field measurements of the wave spectrum (Romero & Melville 2010; Lenain & Melville 2017b; Lenain & Pizzo 2020), illustrated in fig. 4a.

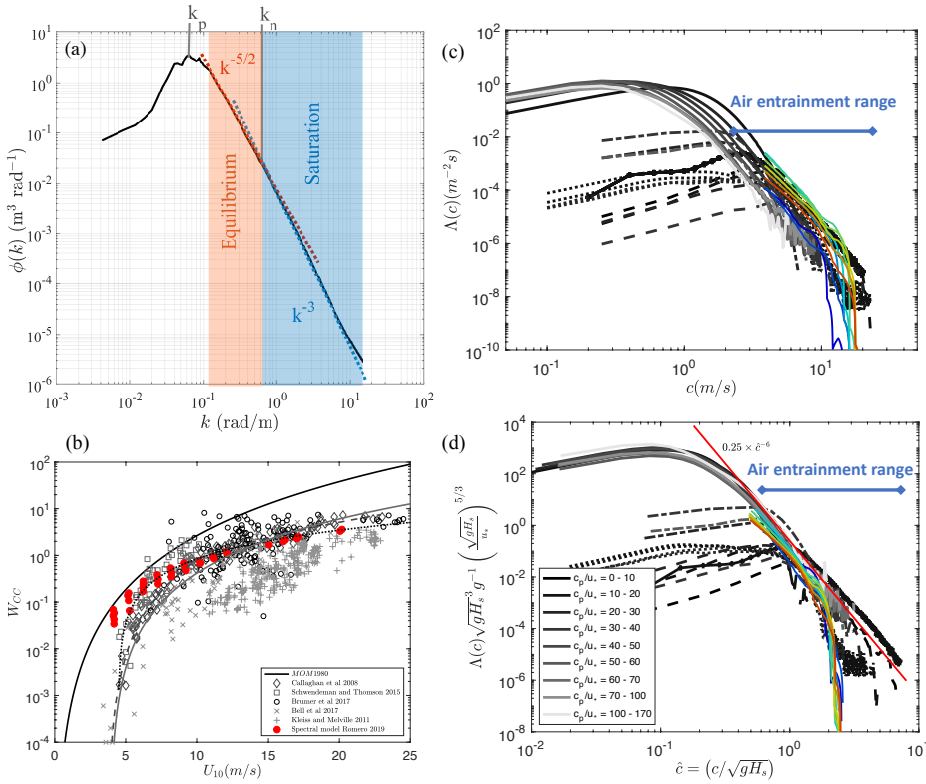

Figure 4

Measurements and spectral modeling of the wave and wave breaking statistics. (a) Example of the omnidirectional wave spectrum, measured for aircraft using LIDAR (Lenain & Melville 2017b; Lenain & Pizzo 2020), illustrating the equilibrium and saturation ranges (with permission from Lenain & Pizzo (2020)). (b) Whitecap coverage from field measurements (Callaghan et al. 2008; Kleiss & Melville 2010; Schwendeman & Thomson 2015; Brumer et al. 2017b) and modeled from $\Lambda(c)$ (Romero 2019), with some empirical parameterization indicated. A large scatter in the data remain. (c) $\Lambda(c)$ from field experiments (Gemmrich et al. 2008; Thomson et al. 2009; Kleiss & Melville 2010; Zappa et al. 2012; Sutherland & Melville 2013; Schwendeman et al. 2014; Deike et al. 2017a), with scatter similar to the whitecap coverage in terms of amplitude of $\Lambda(c)$. Note the infra-red measurements extend to the micro-breaker range ($c < 1$m/s) which do not entrain air. Spectral model from (Romero 2019) is in color and encompass the variability observed in the field. (d) Rescaled $\Lambda(c)$ distribution according to eq. 12 significantly reduces the scatter in the data. Adapted with permission from Deike et al. (2017a); Deike & Melville (2018); Romero (2019).

3.2. Breaking waves in the open ocean

3.2.1. Whitecap coverage. Wave breaking at the ocean surface and the associated air entrainment lead to the presence of whitecaps at moderate to high wind speed. The whitecap coverage, W_{CC}, is commonly defined as the white patches of bubbles formed after breaking at the ocean surface (Monahan & Muircheartaigh 1980). Despite its apparent simplicity (one only needs a camera to measure white patches at the surface of the ocean!), their measurement has proven challenging and large scatter in the recent data set still remains, when presented as a function of wind speed only, as shown in figure 4b. The scatter is related in

parts to the dependency of breaking waves on the sea-state, to the local breaking intensity, to the details of the image processing, as well as the possible role of temperature and water contamination on the bubble plume life time (Callaghan et al. 2008; Kleiss & Melville 2010; Schwendeman & Thomson 2015; Brumer et al. 2017b; Callaghan et al. 2017). Since the whitecap coverage provides only a geometric information, relationships to the local wave field is done via empirical relationships. Nevertheless, once provided with a measure, or model of W_{CC}, empirical relationships with the related bubble gas flux, or bubble sea spray production can be proposed (Garbe et al. 2014; Lewis & Schwartz 2004; de Leeuw et al. 2011).

3.2.2. The distribution of length of breaking crest and Phillips (1985) framework. Phillips (1985) introduced the distribution of length of breaking crest, $\Lambda(\mathbf{c})$, with $\Lambda(\mathbf{c})d\mathbf{c}$ the expected length of breaking crest moving between $\mathbf{c}$ and $\mathbf{c}+d\mathbf{c}$, per unit surface area. The azimuth-integrated distribution is $\Lambda(c) = \int \Lambda(\mathbf{c})cd\theta$. This scale by scale representation of the breaking field consists of tracking the breaking fronts, and their speed (see figure 1). The role of breaking waves on air-sea fluxes is then naturally obtained through the moments of $\Lambda(\mathbf{c})$. The zeroth moment gives the total length of breaking fronts (per unit surface ocean area), $L = \int \Lambda(\mathbf{c})d\mathbf{c}$. The first moment gives the fraction of total surface area turned over per unit time, $R = \int c\Lambda(\mathbf{c})d\mathbf{c}$. The whitecap coverage is dimensionally given by $W_{CC} = \int \tau c\Lambda(\mathbf{c})d\mathbf{c}$, where τ is the characteristic whitecap lifetime, which can be related to the breaking scales by $1/\tau \propto ck$, which leads to the second moment, $W_{CC} \propto \int c^2\Lambda(\mathbf{c})d\mathbf{c}$. This formulation naturally contains sea-state variability of the whitecap coverage through the sea state variability of the $\Lambda(c)$ distribution (Kleiss & Melville 2010; Romero 2019). The fourth moment relates to the momentum flux, while the fifth moment gives the energy dissipation due to breaking waves per unit surface area,

$$M = \int \frac{b\rho}{g} c^4 \Lambda(\mathbf{c})d\mathbf{c} \quad S_{diss} = \int\int \frac{b\rho}{g} c^5 \Lambda(\mathbf{c})d\mathbf{c}. \tag{11}$$

where b is the breaking parameter (see §2, and Duncan (1981); Phillips (1985)).

The breaking parameter has been shown to depend on the breaking slope (§2). Romero et al. (2012) proposed to estimate the local slope from the saturation spectrum, $hk \equiv \sqrt{B(k)} = \sqrt{\phi(k)k^3}$, to obtain a spectrally defined breaking parameter $b(k) = A_T(\sqrt{B(k)} - \sqrt{B_T})^{5/2}$, where A_T is a non-dimensional coefficient and B_T a breaking threshold. The coefficients A_T and B_T have orders of magnitude constrained by laboratory experiments and values adjusted to balance the wind input term used in spectral models (Romero et al. 2012; Romero 2019). Sutherland & Melville (2013, 2015) performed field measurements, jointly measuring the sea surface breaking statistics and the near surface upper ocean using underwater turbulence acoustic sensors to demonstrate that this framework allows to close the energy and momentum budget under a breaking wave field.

Following the work by Longuet-Higgins (1957), Romero & Melville (2011); Romero (2019) related the breaking statistics to the wave spectrum, by assuming proportionality between the breaking statistics with the statistics of crest lengths exceeding a wave slope criterion. The breaking statistics in the k-space is then written as $\Lambda(\mathbf{k}) = \frac{l}{k}\exp(-B_{br}/B(\mathbf{k}))M_L(\mathbf{k})M_W(k))$, where M_W is a wind modulation function, M_L a longer waves modulation to breaking, and B_{br} a breaking threshold parameter. Romero (2019) used this within spectral wave models and obtained a modeled distribution of the breaking statistics fully compatible with field measurements of $\Lambda(c)$, and realistic whitecap coverage, validating this spectral modeling approach (see fig. 4c,d).

H_s: is the significant wave height, defined from the wave spectrum $H_s = 4\sqrt{\phi(k)dk}$.

c_p: is the phase speed at the peak of the wave spectrum k_p, with the gravity waves linear dispersion relation in deep water $c_p = \sqrt{g/k_p}$.

$S = hk \equiv \sqrt{B(k)} = \sqrt{\phi(k)k^3}$: relates the local breaking slope to the saturation spectrum, connecting the results from canonical breaking waves to the field description.

3.2.3. Measuring and scaling $\Lambda(c)dc$. Phillips (1985) proposed dimensional arguments to describe the shape of the breaking distribution, based on equilibrium between energy dissipation and wind input, leading to $\Lambda(c) \propto g u_*^3 c^{-6}$.

The potential of the $\Lambda(c)$ framework to estimate the energy, momentum and mass transfer between the ocean and the atmosphere has motivated measurements using infra-red and visible cameras, from research vessels/platforms (Gemmrich et al. 2008; Thomson et al. 2009; Zappa et al. 2012; Sutherland & Melville 2013; Schwendeman et al. 2014), and from aircraft (Kleiss & Melville 2010) with discussion on the processing methodologies (Banner et al. 2014). Overall, these field measurements have confirmed the $\Lambda(c) \propto c^{-6}$ scaling over a wide range of scales, while also highlighting a more complex dependency on fetch and wave age (see figure 4c). Sutherland & Melville (2013) proposed the following scaling, $\frac{\Lambda(c)c_p^3}{g} = \hat{K}\left[\frac{c}{\sqrt{gH_s}}\left(\frac{gH_s}{c_p^2}\right)^{1/10}\right]^{-6}\left(\frac{u_*}{c_p}\right)^{1/2}$, with $\hat{K} \approx 0.05$ a non-dimensional constant fitted to the data. A key success in this result is to rescale c by $\sqrt{gH_s}$ a characteristic speed accounting for the breaking strength and inspired by the scales of turbulent motion under breaking waves (see §2). Deike & Melville (2018) pointed out the weak $\left(gH_s/c_p^2\right)^{1/10}$ dependency, and used the fetch limited relationship, $gH_s \propto c_p^2$, to propose a simplified scaling

$$\frac{\Lambda(c)\sqrt{gH_s}^3}{g} = K\left(\frac{c}{\sqrt{gH_s}}\right)^{-6}\left(\frac{u_*}{\sqrt{gH_s}}\right)^{5/3}, \tag{12}$$

where $K \approx 0.25$ a fitted non-dimensional constant, shown in fig. 4c to collapse all data within an order of magnitude.

3.3. Air flux over an ensemble of breaking waves

We now consider the air bubble flux into the water associated with breaking, combining the breaking distribution and the individual entrainment described in §2. This will be central to the scale-dependent estimation of bubble mediated gas flux and sea spray generation by bubble bursting. Deike et al. (2017a) defines the rate of entrainment of air per unit area of ocean surface, V_A (units of a volume per area per time),

$$V_A = \int v_l(c)\Lambda(c)dc, \text{ with } v_l(c) = V/(L_c\tau_b), \tag{13}$$

V_A: is the entrained air bubble volume flux entrained, given by the third moment of $\Lambda(c)$ and the wave breaking strength.

where $v_l(c)$ is the volume of air entrained by breakers moving at a speed between c and $c + dc$, per unit time, per unit length of breaking crest. It is given by the volume of air entrained by a single breaker V (eq. 7), and the plume life-time, $\tau_b \propto h/W$, so that

$$V_A = \int B\frac{b}{(hk)}\frac{c^3}{g}\Lambda(c)dc. \tag{14}$$

The volume of air entrained by breaking waves (which is the volumetric analog of the whitecap coverage) is therefore given by the third moment of $\Lambda(c)$, modulated by a factor that depends on the breaking strength, as well as the ratio of work done by buoyancy forces and mechanical dissipation. Using eq. 3, we have $V_A = \int Bs(k)^{3/2}\frac{c^3}{g}\Lambda(c)dc$, where $s(k) \approx hk$, and following the work done on energy dissipation, we consider $b/hk = s(k)^{3/2} = A_T(\sqrt{k^3\phi(k)} - \sqrt{B_T})^{3/2}$ using the same constants A_T and B_T as for energy dissipation.

The volume flux V_A can then be estimated by knowledge of the breaking statistics $\Lambda(c)$, and wave spectrum $\phi(k)$, for any wave state, in the presence of swells and wind waves.

Note that open ocean measurements of the volume flux under breaking waves are extremely challenging, and a direct validation of eq. 14 in the field is lacking. This formulation of the total air bubble flux will be validated a-posteriori when considering the associated gas and sea spray fluxes (involving other assumptions and models), in §4 and 5.

4. From the atmosphere to the ocean: bubble mediated gas transfer.

4.1. Challenges in estimating the gas transfer velocity

Gas transfer at the ocean surface is of paramount importance, with ocean uptake accounting for approximatively 30% of the carbon dioxide (CO_2) released into the atmosphere (Friedlingstein et al. 2020), and about 40% due to air bubbles entrained by breaking waves (Reichl & Deike 2020), while bubbles dominate the gas transfer of low solubility gases such as O_2, key to biological activity (Emerson et al. 2019). The gas transfer between the ocean and the atmosphere is usually represented as (Wanninkhof et al. 2009)

$$F = k_w(C_0 - C_w) = k_w(C_0 - K_0 p_a), \tag{15}$$

with k_w the gas transfer velocity and $C_0 - C_w$ the concentration difference between ocean and atmosphere, the latter sometimes written in terms of the gas partial pressure (p_a, kg m^{-1} s^{-2}) and the gas solubility in seawater (K_0, mol s^2 kg^{-1} m^{-2}). The gas transfer velocity can be measured by dual tracer (Ho et al. 2006, 2011) and eddy covariance techniques (Edson et al. 2011; Bell et al. 2017; Brumer et al. 2017a) with extensive reviews on field measurements by Wanninkhof et al. (2009); Garbe et al. (2014). Traditional parameterizations used in ocean and climate models for the gas transfer velocity, k_w, reflect correlation with windspeed, such as in Wanninkhof et al. (2009); Ho et al. (2006) $k_w^{W14} = C_{W14} U_{10}^2 \, (Sc/660)^{-1/2}$, where Sc is the Schmidt number ($Sc = \nu/D$, which compares the water kinematic viscosity, ν, to the gas diffusivity, D, U_{10} is ten-meter wind speed, and C_{W14} an empirical constant constrained using bulk field observations, global inventories and tracer budget experiments (Wanninkhof et al. 2009; Wanninkhof 2014). The power dependence on U_{10} (here quadratic) is an empirical result taken when considering mean wind speed dependence in field studies, and is supposed to encompass the role of turbulence, as well as bubbles in increasing the transfer velocity at high wind speed. As shown in fig. 5a, recent open ocean gas transfer velocity measurements of CO_2 and dimethyl sulfide (DMS) display very large scatter, when analyzed as a function of wind speed (Miller et al. 2009; Edson et al. 2011; Brumer et al. 2017a; Bell et al. 2017; Leighton et al. 2018), exposing the failure of wind-speed parameterization at intermediate to high wind speeds that is associated with bubble-mediated gas transfer. Woolf et al. (2019) summarizes the remaining uncertainties in the global carbon uptake by the ocean as coming from uncertainties in spatial measurements of partial pressure difference and modeling of the gas transfer velocity.

k_w: is the gas transfer velocity, measures the transport of gas between the ocean and the atmosphere, and will be a function of the physical parameters controlling the transport, such as wind, turbulence, bubbles, gas diffusivity and solubility.

Separating the contribution to the total flux into the bubble gas transfer and the diffusive transfer at an unbroken surface, bubble-mediated gas transfer has been introduced as a function of the whitecap coverage (Woolf & Thorpe 1991; Keeling 1993; Woolf 2005). The COAREG framework, a sophisticated model that uses such decomposition, has been widely used to try to reproduce field measurements (Fairall et al. 2003; Edson et al. 2011; Bell et al. 2017). However, all the wave information is lost when considering the whitecap coverage empirical formulation with wind speed, which limits comparison between different sea-state configurations, and is hidden in the uncertainties of the coefficients in COAREG. In an effort to collapse available field data, parameterizations using wind and significant wave

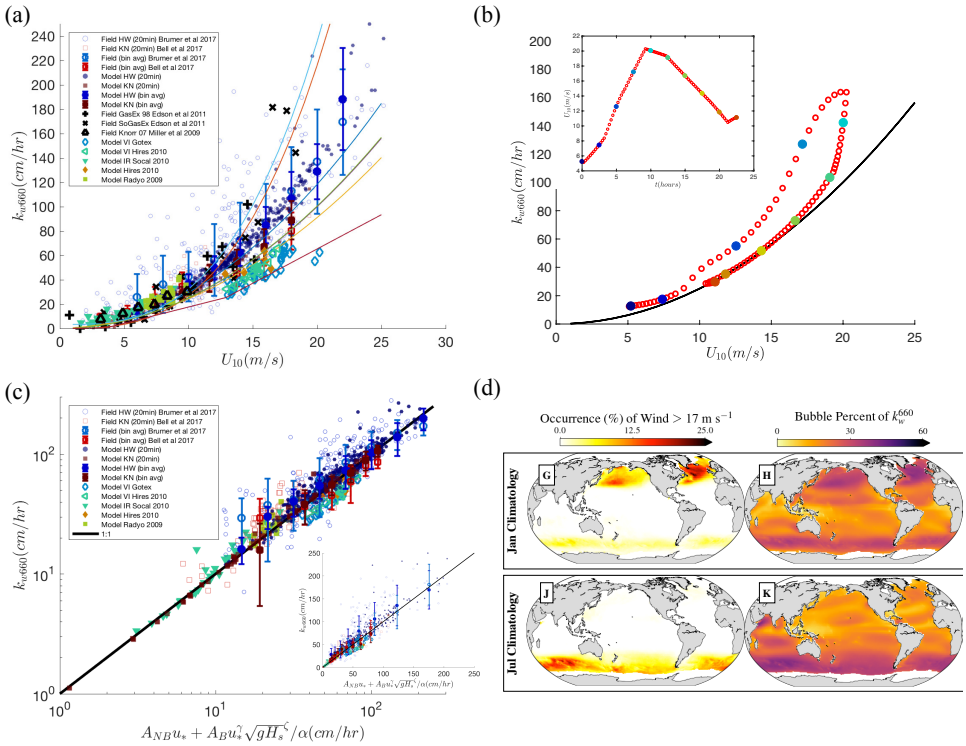

Figure 5

(a) Gas transfer velocity for CO_2, k_{w660} as a function of U_{10}, for multiple field campaigns (symbols) and wind only parameterizations in solid lines (quadratic and cubic). Large scatter in the data is observed. Data from Brumer et al. (2017a); Bell et al. (2017) are open blue and red symbols and the modeled data (eq. 21, (Deike & Melville 2018)) for these conditions are full symbols (Small are 20 min averaged data, large are bin-averaged with wind speed). The model reproduces the field measurements with good accuracy given the complexity of the processes. (b) Spectral gas transfer velocity k_w (eq. 21) during a single 24 hours storm in the Southern Ocean (inset shows wind as a function of time, the colored markers indicate the time-evolution and storm intensification and set-down), modeled using WW3, illustrating sea-state induced variability on the gas transfer velocity, with up to a factor 2 difference at the same wind speed between the storm intensification stage and the set-down. Original data. (c) Semi-empirical formulation (eq. 23) for the gas transfer velocity for CO_2 and DMS, $k_{w660} = \left(A_{NB}u_* + A_B(u_*^{5/3}\sqrt{gH_s}^{4/3})/\alpha\right)$, and $A_B = \tilde{A_B}(Sc/660)^{1/2}$, where $\tilde{A_B} = 1.1 \pm 0.3 \times 10^{-5}$ m^{-2}s^2 is the only fitted parameter. Main figure is log-scaled while inset is linearly scaled and display a good collapse of the data (Deike & Melville 2018). (d) Contribution of bubble gas transfer velocity obtained from global WW3 simulations and using eq. 23, January and July averaged over 30 years (1985-2015), showing that bubbles account for up to 50% of the k_w for CO2 at high latitude in winter time, corresponding to high frequency events of wind speed over 17 m/s. Adapted with permission from Deike & Melville (2018) (a,c) and Reichl & Deike (2020) (d).

height have been proposed, showing a reasonable collapse, with empirical coefficients for CO_2 and DMS (Brumer et al. 2017a). Another effort is to use the turbulence dissipation rate in the water as a better proxy for gas transfer (Esters et al. 2017).

The case of low solubility gases for which the bubble mediated gas transfer is even more important (Keeling 1993; Emerson & Bushinsky 2016; Leighton et al. 2018) is especially challenging, with the separate role of large and small bubbles, the latter bringing an asymmetric contribution (Woolf & Thorpe 1991; Leighton et al. 2018). There is currently no consensus on the gas transfer velocity formulation to be used in large scale models for O_2 and N_2. Atamanchuk et al. (2020) recently showed that using different models for k_w leads to variations of orders of magnitude and even change of sign of the flux in certain high wind speed events, linked to the representation (or lack) of the asymmetric bubble contribution. As such, significant disagreement between empirical formulations and field measurements of N_2 and O_2 fluxes remain (Stanley et al. 2009; Emerson & Bushinsky 2016; Emerson et al. 2019; Liang et al. 2017; Atamanchuk et al. 2020).

4.2. Gas transfer velocity

The present section discusses bubble mediated transfer models and their integration within a sea-state dependent gas transfer velocity formulation. We start by writing the flux as (Keeling 1993; Woolf & Thorpe 1991),

$$F = F_{nb} + F_b. \tag{16}$$

separating the non-breaking, F_{nb}, and bubble mediated, F_b, gas fluxes contributions.

4.2.1. Unbroken flux and gas transfer velocity. F_{nb} is driven by diffusive mass transfer at the unbroken air-sea interface, enhanced by turbulence. Following eddy-renewal theory, F_{nb} scales with $Sc^{-1/2}$ and linearly with the friction velocity u_* (Garbe et al. 2014),

$$F_{nb} = k_{nb}(C_0 - C_w), \text{ with } k_{nb} = A_{nb} u_* \left(\frac{Sc}{660}\right)^{-1/2}. \tag{17}$$

The non-dimensional coefficient A_{nb} is empirical and varies by about 20 to 30% in the literature, depending on whether CO_2 or DMS data at relatively low wind speed are used as constraints (Woolf 2005; Fairall et al. 2003; Edson et al. 2011). The scaling in friction velocity is equivalent to the one involving the turbulent dissipation rate, $k_{nb} \propto Sc^{-1/2}(\nu\varepsilon)^{1/4}$ (Zappa et al. 2001; Garbe et al. 2014). While the turbulence is a more direct controlling factor of the gas transfer than the friction velocity, systematic measurements just below the free surface remain challenging. Note also that the unbroken transfer could depend on the surface wave conditions, which could be estimated through the turbulence dissipation term, or could be estimated via a sea-state dependent drag coefficient C_D that links the wind speed at 10 meters and the friction velocity.

4.2.2. Bubble gas transfer models. The bubble flux F_b can be written as the sum of two terms: one representing bubbles with the ability to flux in or out depending on the concentration gradient, written as $k_b(C_0 - C_w)$, where k_b is the bubble gas transfer velocity. The second term represents the asymmetric pathway from small bubbles fully dissolving in the water column. The size cut-off for these small bubbles is estimated between 50 to 300μm depending on the models, corresponding to bubbles with rise velocities smaller than the water turbulence fluctuations, hence not able to rise back to the surface and that will eventually collapse due to hydro-static and surface tension pressure.

Woolf & Thorpe (1991) writes $F_b = k_b(C_0(1+\delta) - C_w)$, with δ the asymmetric contribution. Breaking waves are directly controlling bubble gas transfer velocity through air entrainment and earlier formulations have used the whitecap coverage as a large scale constraints, with $k_b \propto W_{CC}$. The bubble dynamics in the upper turbulent ocean is then treated in a Lagrangian way, with various levels of complexity. It involves an injected bubble size distribution $Q(R_b)$, a modeled bubble rise velocity, $w_b(R_b)$, together with individual gas transfer bubble velocity, $\kappa_b(R_b)$. The upper ocean dynamics is modeled through its background turbulence velocity, and can account for idealized Langmuir circulation to consider deeper entrainment of small bubbles (Leighton et al. 2018). As discussed by Leighton et al. (2018); Emerson & Bushinsky (2016); Emerson et al. (2019); Liang et al. (2017), the asymmetric pathway is especially important for low solubility gases like N_2 and O_2 but has also been proven important at high wind speed for CO_2 (Leighton et al. 2018).

The gas exchange model from Woolf & Thorpe (1991) has been recently combined with large eddy simulations of the upper ocean (Liang et al. 2011, 2012, 2017), including the stochastic forcing resulting from realistic breaking wave statistics (Liang et al. 2017). This formulation has provided the most detailed description of the role of bubbles in storms, for CO_2, N_2 and O_2, and has demonstrated the non-trivial role of bubbles in enhancing or limiting gas exchange, together with non-linear hysteresis cycles when wind speed increases or decreases (Liang et al. 2017). This approach presents the key advantage of integrating complex upper ocean processes such as entrainment of bubbles by Langmuir circulation to greater depth, which would result in much longer residence time (Liang et al. 2012). The downside is that the full sea-state dependent LES requires high resolution computations, which is usually too expensive to extend to ocean scales and limits the assessment of the importance of gas exchange sea-state variability on large scale and long term patterns.

The original bubble mediated gas model from Keeling (1993) also separates the contribution of small and large bubbles and the flux is written as

$$F = F_{nb} + F_b = (k_{nb} + k_b)(C_o - K_0 p_a) + k_b^{asym} K_0 p_a. \tag{18}$$

Keeling (1993) discusses the resulting super-saturation for major gases, while arguing that large bubbles are important for CO_2 gas exchange. The contribution of large bubbles is related to the total air bubble flux, $k_b = \int dR_b (4\pi/3) R_b^3 Q(R_b) E(R_b)/\alpha$, where $E(R_b)$ is a size-dependent efficiency coefficient which estimates in an integrated way the amount of gas transferred by each bubble, $Q(R_b)$ the bubble flux and α the (non-dimensional) Ostwald gas solubility. In Keeling (1993), the entrained volume flux $V_A = \int dR_b (4\pi/3) R_b^3 Q(R_b)$ was estimated from the whitecap coverage $V_A \propto W_{CC}$. The efficiency coefficient is written in terms of the depth of bubble injection z_0, and an equilibration depth $H_{eq}(R_b)$,

$$E(R_b) = \frac{z_0}{z_0 + H_{eq}(R_b)}, \text{ and } H_{eq}(R_b) = \frac{4\pi}{3\alpha} \frac{R_b w_b(R_b)}{\kappa_b(R_b)}, \tag{19}$$

where $\kappa_b(R_b)$ is the individual bubble exchange rate with the surrounding water and z_0 the bubble injection depth. These equations provide a depth integrated estimation of the gas exchange by bubbles, within a turbulent background. The equilibrium depth $H_{eq}(R_b)$ can be interpreted as the depth at which the bubble will exchange all of its gas content. This formulation is simple, once provided with accurate models of the input bubble size distribution, rise velocity, individual exchange coefficient and injection depth.

The asymmetric term is written as $k_b^{asym} K_0 p_a$ (Keeling 1993), and expressed as $k_b^{asym} = V_{inj}/\alpha + \Delta P/P_0 \int dR_b (4\pi/3) R_b^3 Q(R_b) E(R_b)/\alpha$, where V_{inj} is the volume of the small bubbles which are assumed to completely dissolve. The second term is related to the average

depth of the bubble plume, and can be written as $\Delta P/P_0 \int dR_b(4\pi/3)R_b^3 Q(R_b)E(R_b)/\alpha = \int dR_b(4\pi/3)R_b^3 Q(R_b)F(R_b)/\alpha$ where $F(R_b) = \frac{H_{eq}}{H_0}\frac{z_0^2}{(z_0+H_{eq}(R_b))^2}$. The gas supersaturation can also be estimated from this model (see Keeling (1993)).

4.2.3. Bubble model input: injection depth, rise velocity and transfer rate in turbulence. All bubble mediated gas transfer models require information on the injection depth (z_0), rise velocity ($w_b(R_b)$) and individual bubble exchange rate ($\kappa_b(R_b)$). The rise velocity and individual transfer rates derived for bubbles moving in quiescent flow have been used, for clean and contaminated (dirty) interface (Woolf & Thorpe 1991; Keeling 1993; Levich 1962). However, bubbles entrained by breaking will be subject to a turbulent flow, modifying their velocity and transfer rate. I briefly summarize some results of this vast topic, which stresses the role of the turbulent fluctuations on the bubble residence time and individual gas exchange velocity, and should be integrated to air-sea bubble gas exchange models.

The injection depth can be estimated as the breaking height, $z_0 \sim h$ supported by laboratory experiments and simulations (Lamarre & Melville 1991; Deane & Stokes 2002; Deike et al. 2016; Callaghan et al. 2013), and some field measurements (Bowyer 2001; Lenain & Melville 2017a). We note the difficulty in measuring the bubbles next to the surface in the field, which would deserve further measurements, combined with breaking observations.

The rise of bubbles in a turbulent background remains poorly understood with size dependent effects of the turbulent background on the drag and lift forces of the bubbles. Most experimental and numerical studies have reported a slow down compared to the rise velocity in quiescent water, varying from 20% to 70%, mainly controlled by the relative intensity of the turbulent fluctuations u_{rms} and the quiescent bubble velocity, while complex coupling with the mean flow limits comparison between data sets (Poorte & Biesheuvel 2002; Aliseda & Lasheras 2011; Salibindla et al. 2020; Ruth et al. 2021).

The turbulent flow surrounding the bubbles will modify the individual bubble diffusive gas exchange, by changing the characteristic time scale of eddy renewal, $\tau_t \propto R_b/\tilde{w}$, where $\tilde{w}$ is a turbulent velocity (either the rise velocity in turbulence, or the turbulent fluctuations u_{rms}), leading to a transfer rate $\kappa_b \propto \sqrt{D\tilde{w}/R_b}$ similar to the result in quiescent water but now accounting for a turbulent velocity (Farsoiya et al. 2021).

4.3. Sea state dependent bubble mediated gas transfer velocity

Deike et al. (2018) combined the description of air entrainment and bubble population discussed in §2 and 3 with the model from Keeling (1993) to account for the sea-state effects on the bubble mediated gas transfer velocity k_b (but did not consider asymmetric effects). The bubble-mediated transfer is controlled by the size distribution of bubbles being entrained (written as a number per unit ocean surface area per unit time), $Q(R_b)$,

$$Q(R_b) = \int q_l(R_b, c)\Lambda(c)dc, \text{ with } q_l(R_b, c) = \frac{B}{2\pi}s(k)^{3/2}N(R_b)\frac{c^3}{g}, \tag{20}$$

where $q_l(R_b, c)$ is the size dependent bubble flux per unit length of breaking crest. The bubble size distribution $N(R_b)$ is described in §2. For bubbles larger than the Hinze scale, $R_b > R_H$, containing 95% of the volume $N(R_b) \propto R_b^{-10/3}$, while for $R_b < R_H$, $N(R_b) \propto R_b^{-3/2}$, so that the total volume of air entrained is given by the large-scale constraints on the total volume flux, eq. 14 and $0.95V_A = \int_{R_H}^{R_M} dR_b Q(R_b)\frac{4\pi}{3}R_b^3$. The bubble gas transfer velocity k_b is then written as (Deike & Melville 2018)

$$k_b = \iiint dcdR_b f_l(R_b, c)\Lambda(c), \text{ with} \tag{21}$$

$$f_l(R_b, c) = \frac{4\pi r^3}{3}\frac{q_l(R_b, c)E(R_b)}{\alpha} = \frac{B4\pi r^3}{6\pi}\frac{s(k)^{3/2}c^3}{g}\frac{N(R_b)E(R_b)}{\alpha}. \tag{22}$$

This equation yields a bubble gas transfer velocity that combines the bubble mediated transfer estimated from the physicochemical properties of the gas (solubility, diffusivity, viscosity) and the wave and wave-breaking statistics.

A mechanistic understanding of the sea-state variability can then be explored by considering spectral wave model, such as WAVEWATCHIII (WW3) (Ardhuin et al. 2010) to simulate wave spectrum, combined with the breaking modeling from Romero (2019) to compute $\Lambda(c)$ from the wave spectrum, and the gas transfer model from Deike & Melville (2018), yielding integration of eq. 22. We consider a typical winter storm in the Southern Ocean in figure 5b, with wind increasing from 5 to over 20 m/s in a few hours. We observe values of k_w up to a factor 2 higher during the storm intensification than during the set-down in the next 10 hours, which rationalizes some of the observed variability in field measurements of k_w (shown in fig. 5a).

4.4. Simple parameterization for gas transfer and global estimations.

The large scale ocean and climate communities are widely using the classic wind only formulations, e.g. Wanninkhof et al. (2009), and apply the results to other gases by considering only the role of the Sc number. This approach is insufficient as demonstrated by various studies on low solubility gases (Atamanchuk et al. 2020; Emerson et al. 2019; Liang et al. 2017) or for CO2 during high frequency storms (Leighton et al. 2018). However, the overhead in computation cost induced by a wave model coupled with large scale ocean and climate models remains high. This motivates simple semi-empirical formulations, of the form $k_b = F(u_*, H_s, c_p, Sc, \alpha)$, valid for multiple gases, without having to re-tune the empirical coefficients. Such parameterizations could be used with wave climatology, as well as incoming satellite products (e.g. SWOT), which will provide global coverage of the significant wave height H_s.

Deike & Melville (2018) proposed such a parameterization for the bubble mediated gas transfer velocity, air-sea gas transfer velocity, derived from eq. 22, as a function of u_* and H_s. It captures the main wave effect, as well as solubility and diffusivity, and collapse all available data for CO_2 and DMS, as shown in fig. 5c (but does not account for bubble asymmetric effects, which would be necessary for O_2 and N_2),

$$k_w^{simple} = k_{nb} + k_b^{simple}, \text{ with } k_b^{simple} = \left(\frac{A_B}{\alpha}\left[u_*^{5/3}\sqrt{g H_s}^{4/3}\right]\right)\left(\frac{Sc}{660}\right)^{-1/2}. \tag{23}$$

Reichl & Deike (2020) used this formulation to estimate the potential role of sea-state variability on gas transfer at the regional and global scales by running global wave simulations with WW3, combined with products reconstructing the CO2 partial pressure difference. They estimated that the bubble mediated CO_2 transfer accounts for about 40% of the total flux, with significant seasonal and regional variability, dominating the gas transfer velocity at high latitude in winter seasons due to the occurrence of multiple high wind speed events, as illustrated by monthly averaged maps on fig. 5d. The role of such sea-

state dependent variability in global geochemical cycle remains to be tested, with potential implications in deeper water mass formation and composition.

5. From the ocean to the atmosphere: spray generation by bubble bursting

Ocean spray is composed of small liquid droplets formed through two main pathways: the spume drops, produced from the tearing of breaking wave crests by strong winds (Veron et al. 2012; Erinin et al. 2019; Ortiz-Suslow et al. 2016; Troitskaya et al. 2018), recently reviewed by Veron (2015) and which I will not further discuss. The second mechanism for drop generation is by bursting bubbles, through two processes sketched in fig. 1: film (Blanchard 1963; Lhuissier & Villermaux 2012) and jet drops (Spiel 1994, 1997; Ghabache et al. 2014; Deike et al. 2018). These droplets can then be transported to the upper atmosphere (Mueller & Veron 2009; Richter et al. 2019), where they may evaporate, affect the radiative balance of the atmosphere and serve as cloud condensation nuclei (Lewis & Schwartz 2004; de Leeuw et al. 2011). The heat and momentum fluxes at the ocean-atmosphere interface are strongly modulated by sea spray, and are major players in weather prediction and hurricane intensification (Veron 2015). These droplets transport water, heat, dissolved gases, salts, surfactants, and biological materials, with their chemical composition affected by the production mechanisms and are the chemical link coupling the ocean and the atmosphere (Prather et al. 2013; Wang et al. 2017; Cochran et al. 2017).

Sea spray generation function: is the size-dependent number of droplets generated per unit area of ocean surface, per unit time

Despite the importance of sea spray aerosol, large uncertainties remain in predicting their size and velocity generation functions (Lewis & Schwartz 2004; de Leeuw et al. 2011; Veron 2015), due to the complexity of their formation, and the large range of scales involved in the production processes, from bubbles bursting at the ocean surface to large scale breaking waves. The role of the sea-state is largely missing in classic parameterization of the sea-spray generation function, while the role of the water contamination and enrichment by biological activity adds an extra layer of complexity, affecting the efficiency of bursting processes (Wang et al. 2017; Frossard et al. 2019; Neel & Deike 2021).

I will present recent advances in our mechanistic understanding of the production of sea spray by bubble bursting, thanks to idealized laboratory and numerical simulations at the bubble scale; and combine them with the description of the wave breaking dynamics (§2) and statistics (§3). This will lead to a physics-based sea spray generation function, which compares favorably with data and source function from the literature.

5.1. Number and size of film and jet drops produced by bubble bursting

Earlier studies (see the reviews of Lewis & Schwartz (2004); Veron (2015)) have identified the two mechanisms sketched in fig. 1. I focus on recent results describing the size, velocity and number of drops ejected by bursting, driven by advances in high speed photography and computational methods. The controlling parameters of jet and film drop production can be understood in terms of characteristic time and length scales, leading to a universal description of the ejection properties which account naturally for variations in -some- ocean water properties. At the scales of drops and bubbles, capillary forces will become dominant, and the influence of gravity can be evaluated by comparing the bubble scale R_b to the capillary length $\ell_c = \sqrt{\gamma/\rho g}$ ($\approx$ 2.7 mm in water). Viscosity has a non-trivial role in selecting the capillary waves during the cavity collapse process, and modulate the film drainage, so that we introduce the visco-capillary length $l_\mu = \mu^2/(\rho\gamma)$, which controls

processes involving cavity collapse and jet formation (Eggers & Villermaux 2008).

Film drops: are ejected during the bubble thin cap film bursting.

5.1.1. Film drops. These are generated by the puncture, retraction and destabilization of the thin cap of bubbles mainly larger than the capillary length $R_b > \ell_c$. They are produced between $0.4l_c$ and $3.8l_c$ in tap water (Lhuissier & Villermaux 2012), coherent with various work in salt water where film drops are observed from bubbles ranging from 1mm to 10mm (Blanchard & Syzdek 1988; Resch & Afeti 1991; Cipriano & Blanchard 1981). The retraction velocity of the film is given by the Taylor-Culick velocity, $V_{TC} = \sqrt{2\gamma/\rho h_b}$, where h_b is the film thickness at bursting. Lhuissier & Villermaux (2012) performed extensive laboratory experiments, illustrated in fig. 6, with a description of the film dynamics, leading to its rupture, linking the film drainage and the associated broad-life-time statistics. Once the film ruptures, the cap retracts and destabilizes, following a capillary driven fragmentation pattern, with the mean film drop size found to scale as $\langle r_d \rangle \propto R_b^{3/8} h_b^{5/8}$, varying from 1 microns to 0.5mm, as the film thickness h_b at rupture varies from 0.1 to about 50 microns (Lhuissier & Villermaux 2012). At relative humidity of 80%, this leads to the smallest mean drop around $r_d^{80} \approx 0.5\mu$m (using $r_d^{80\%} = 0.5 r_d$). The mean number of film drops is described by $n_{film}(R_b) \propto (R_b/l_c)^2 (R_b/h_b)^{7/8}$, so that larger bubbles produce on average more film drops. The minimal film thickness in ocean water conditions is probably related to Marangoni instabilities which will systematically lead to film rupture for h_b above 0.1μm, while films fully covered by surfactants might reach smaller sizes (Néel & Villermaux 2018).

h_b: is the cap film thickness at bursting and controls the film drop sizes.

Dry and liquid aerosol sizes:: the dry salt aerosol diameter (D_d^{dry}) can be related to the drop size at 80% ($r_d^{80\%}$) humidity and the initial ejected liquid drop radius (r_d) by $2D_d^{dry} \approx 2r_d^{80\%} \approx r_d$.

Separately, numerous measurements have reported solid dry particles (sea salt aerosols) with diameter down to 0.01μm attributed to film drops (Cipriano & Blanchard 1981; Resch & Afeti 1991; Sellegri et al. 2006; Mårtensson et al. 2003; Wang et al. 2017). The conversion factor between dry solid salt particles and liquid droplets is usually $2D_d^{dry} = 2r_d^{80\%} = r_d$ (see (Fitzgerald 1975; Lewis & Schwartz 2004)). Below $D_d^{dry} \sim 0.1\mu$m, the sea spray aerosols are mainly of organic composition (Quinn et al. 2015; Bertram et al. 2018), their size not directly proportional to the liquid drop size contrary to the sea salt aerosols, so that the smallest liquid drop of 0.5μm is compatible with a smallest dry salt aerosol of 0.1μm.

The film drop production can be described by a coalescence like fragmentation scenario (Villermaux 2020), leading to a size distribution described by a Gamma distribution. Such distribution is a two-parameter function controlled by the mean drop size $\langle r_d \rangle$ and its order m, which is controlled by the roughness of the ligaments during fragmentation (with m=11 used to fit experimental data in Lhuissier & Villermaux (2012), fig. 6),

$$\mathcal{P}(r_d/\langle r_d \rangle) = \frac{m^m}{\Gamma(m)} \left(\frac{r_d}{\langle r_d \rangle} \right)^{m-1} e^{-m \frac{r_d}{\langle r_d \rangle}}. \tag{24}$$

Jet drops: are ejected when a jet forms from the bubble cavity collapse.

5.1.2. Jet drops. These are produced when the bubble cavity collapses and forms a vertical upward jet that destabilizes into drops. The cavity collapse is driven by the focusing capillary waves, leading to the jet ejection, with the wave propagation characterized by the inertio-capillary timescale $\tau_c = \sqrt{\rho R_b^3/\gamma}$, at the scale of the bubble radius R_b.

The use of high speed cameras has led to very detailed and accurate experimental data of the jet drop production process (Ghabache et al. 2014; Ghabache & Séon 2016; Brasz et al. 2018). Separately, Duchemin et al. (2002) presented the first direct numerical simulations of the axisymmetric bubble bursting solving for the two-phase Navier-Stokes equations, and demonstrated that the main controlling parameter of the speed and size of the first ejected droplet is the ratio of the surface tension and viscous forces (as estimated

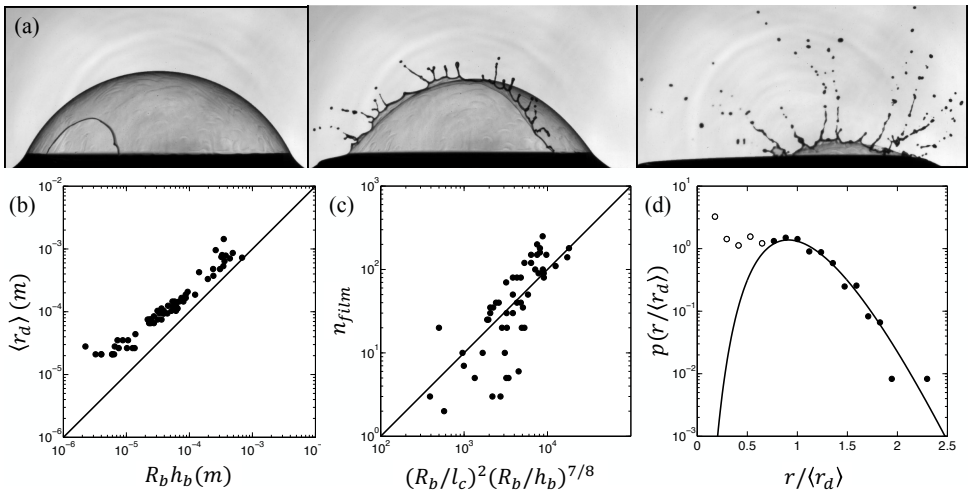

Figure 6

(a) Visualization of the film drop production by bubble bursting. (b) Resulting mean film droplet size, as a function of the bubble radius and film thickness, $\langle r_d \rangle \propto R_b^{3/8} h_b^{5/8}$. (c) Number of film droplet produced, as a function of bubble size, film thickness at bursting and capillary length $n_{film}(R_b) \propto (R_b/l_c)^2 (R_b/h_b)^{7/8}$. (d) Distribution of film droplet size ejected by a bubble bursting event, described by a Gamma distribution (eq. 24), of order 11. (adapted with permission from Lhuissier & Villermaux (2012)).

by the Laplace or Ohnesorge number): $\mathrm{La} = R_b/l_\mu = \frac{\rho\gamma R_b}{\mu^2}$. These simulations showed that there exists an optimal Laplace number around 1000 (about 20μm for salt water at 20 degrees) for which jet focusing is the most efficient and leads to the ejection of very fast, tiny droplets (several tens of m/s for O(1μm) drop). Direct numerical simulations, validated against laboratory data (Deike et al. 2018; Brasz et al. 2018; Berny et al. 2020) (see fig. 7), further demonstrated the universal behavior of the first ejected droplet size and velocity, for a range of Laplace numbers from 900 to 100000, which corresponds to the range of existence of jet drops in salt-water, for bubbles from 10 microns to 3mm (at 20C), the jet and cavity following a self-similar inertio-capillary dynamic (Lai et al. 2018). The optimal Laplace number corresponds to the most effective focusing, with shorter (and slower) capillary waves damped by viscosity, so that the system is controlled by the fastest capillary wave. At higher R_b/l_μ (as well as higher R_b/l_c), the presence of several capillary waves leads to an imperfect focusing, slowing the jet formation, and reducing the efficiency in drop production. These results inspired Gañán-Calvo (2017) to develop a set of scaling laws based on the momentum and energy balance during the cavity reversal process, and under the assumption that the key mechanism for ejection is the focusing of the most effective among the fastest capillary waves produced by the retraction of the cavity. The first drop size r_{d1} and velocity V_{d1} are then given by (with $V_\mu = \gamma/\mu$)

$$\frac{V_{d1}}{V_\mu} = k_v \left(\mathrm{La} \left(\mathrm{La}_\star^{-1/2} - \mathrm{La}^{-1/2} \right) \right)^{-3/4} ; \frac{r_{d1}}{l_\mu} = k_r \quad \sqrt{\mathrm{La}} \quad \sqrt{\frac{\mathrm{La}}{\mathrm{La}_*} - 1} \Bigg) \Bigg)^{5/4} . \tag{25}$$

In these scalings, $La_* \approx 550$ is the drop ejection threshold, while k_r and k_v are empirical

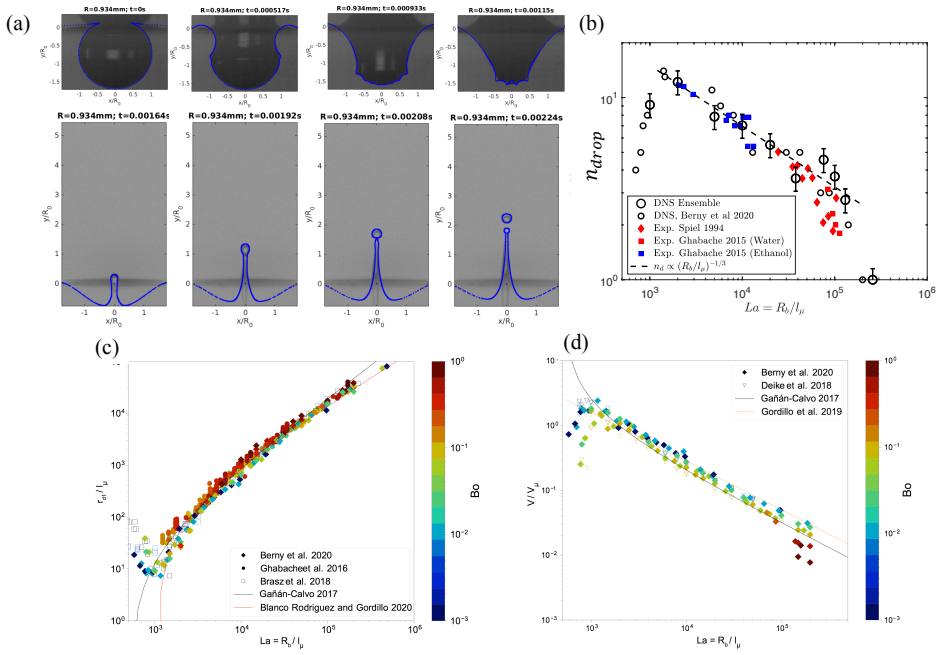

Figure 7

(a) Example of jet drop dynamic, from experiments (photographs) and direct numerical simulations (blue line) for a $\sim$ 1mm bubble in water, displaying excellent agreement in the cavity collapse and jet formation. (b) Number of jet drop ejected as a function of La $= R_b/l_\mu$, with drops produced for $R_b/l_\mu > 600$, while for $R_b^2/l_c^2 > 1$, no jet drops are being produced. (c,d) The first drop velocity from experiments and simulations (b) and size (c) can be described by universal scalings (eq. 25), with excellent agreement between experiments and numerical simulations. Adapted with permission from Deike et al. (2018); Berny et al. (2020).

La $= R_b/l_\mu = \rho\gamma R_b/\mu^2$: is the bubble Laplace number and controls the production of jet drops size, velocity and number, through selection of the capillary waves during the cavity collapse.

O(1) constants fitted to the data. The asymptotic scaling at high La, for the first drop (or jet) velocity, is then $V_{d1}/V_\mu \propto \mathrm{La}^{-3/4}$, and for the first drop size, $r_{d1}/l_\mu \propto \mathrm{La}^{5/4}$. These scaling laws display excellent agreement with experimental and numerical data, for La from 900 to 10^6 (fig. 7), and illustrate a robust result: knowing the bubble size and water properties, the first drop size and velocity can be predicted through universal scalings of La $= R_b/l_\mu$, which encompass variations in temperature and salinity, through changes in density, viscosity and surface tension. The physical assumption behind these scalings have prompted ample discussions and Gordillo & Rodríguez-Rodríguez (2019); Blanco-Rodríguez & Gordillo (2020) proposed an alternative theory based on capillary focusing and tracking the speed of the capillary waves during the cavity collapse, and an inertio-capillary balance, the final results also describing the experimental and numerical data very well.

Jet drops production is controlled by the ratio of the bubble size over the two characteristic lengths of the problem: R_b/l_μ and R_b/ℓ_c (Walls et al. 2015; Berny et al. 2020). For $R_b/\ell_c > 1$, drop ejection is prevented by the action of gravity, while the other limit for jet ejection is due to viscosity, which damps the waves during cavity collapse and prevents drop ejection for $R_b/l_\mu < 550$. For intermediate R_b/l_μ and R_b/ℓ_c, a non-trivial boundary exists

(Walls et al. 2015), but is not relevant in sea water, as it corresponds to higher viscosities.

Thus, the jet drop production lower bound is $R_b^{low}/l_\mu \approx 550$, with more efficient ejection above $R_b^{low}/l_\mu \approx 900$ which yields $10 < R_b^{low} < 30\mu$m depending on water temperature. Such bubbles create jet drops down to 0.5μm, which has been confirmed experimentally (Wang et al. 2017), so that jet drops should in principle not be disregarded when considering sub-microns sea spray aerosol production (Wang et al. 2017; Berny et al. 2021).

Berny et al. (2021), following Berny et al. (2020) used large ensembles of direct numerical simulations to describe the statistics of jet drop ejection, characterizing the number and size of all jet drops produced when a cavity collapses. These results were validated against data from Spiel (1994, 1997); Ghabache et al. (2014); Ghabache & Séon (2016), and showed that for salt-water conditions, the mean number of jet drops follows $n_{jet}(R_b) \propto (R_b/l_\mu)^{-1/3}$, (so that smaller bubbles lead to more drops, due to the capillary wave selection process and a maximum of about 15 drop being ejected). These simulations showed that the mean drop size follows a scaling similar to the first drop (albeit simplified!), $\langle r_d \rangle \propto l_\mu (R_b/l_\mu)^{5/4}$. The drop size distribution of each ensemble can be approximated by a Gamma distribution (eq. 24), with a low order, $m = 4$ corresponding to the break-up of a relatively smooth jet.

5.2. From single bubble bursting to a sea spray droplet distribution

The size distribution of drops produced by bubble bursting entrained by a breaking wave is obtained by integration over all bubbles (Lhuissier & Villermaux 2012; Berny et al. 2021),

$$\mathcal{N}_d(r_d) = \int_{R_b^{low}}^{R_b^{up}} \frac{q(R_b)n(R_b)}{\langle r_d \rangle (R_b)} p(r_d/\langle r_d \rangle, R_b) dR_b, \tag{26}$$

where $q(R_b)$ is the size distribution of bursting bubbles at the surface, R_b^{low} and R_b^{up} are the lower and upper bound of production of drops through the considered mechanism. We assume that we can use the single bubble bursting results from §5.2; and the bubble size distribution under breaking waves from §2. Defining $\tilde{\alpha}$ and $\tilde{\beta}$ such that $q(R_b)n(R_b) \propto R_b^{-\tilde{\alpha}}$ and $\langle r_d \rangle \propto R_b^{\tilde{\beta}}$, and $\zeta = (\tilde{\alpha} - 1)/\tilde{\beta}$, eq. 26 integrates to (Lhuissier & Villermaux 2012)

$$\mathcal{N}_d(r_d) = \mathcal{A} r_d^{-1-\zeta} \left[\Gamma_{inc}(m + \zeta, m r_d / r_d^{up}) - \Gamma_{inc}(m + \zeta, n r_d / r_d^{low}) \right], \tag{27}$$

where Γ_{inc} is the incomplete Gamma function, $r_d^{up} = \langle r_d \rangle (R_b^{up})$, $r_d^{low} = \langle r_d \rangle (R_b^{low})$, and $\mathcal{A}$ is the combined pre-factor of the various algebraic laws.

Lhuissier & Villermaux (2012) performed the integration for the film drop distribution, with $R_b^{low,film} \approx 1$mm and $R_b^{up,film} \approx 10$mm, so that film drops are produced by super-Hinze scale bubbles with $q(R_b) \propto R_b^{-10/3}$, hence $\zeta = 3/4$ so that $\mathcal{N}_d(r_d)^{film} \propto r_d^{-7/4}$.

Berny et al. (2021) performed the integration for the jet drop distribution, with $R_b^{up,jet} \approx l_c \approx 2.7$mm, so that jet drops are mainly produced by sub-Hinze bubbles, with $q(R_b) \propto R_b^{-3/2}$, hence $\zeta = 2/3$ so that $\mathcal{N}_d(r_d)^{jet} \propto r_d^{-5/3}$. Note that in principle $R_b^{low}/l_\mu \approx 900$ (10 to 30 microns depending on temperature), and would lead to sub-microns jet drops; but bubbles below 50 to 200 microns have rise velocity O(1cm/s) and might never reach the surface due to the turbulent background.

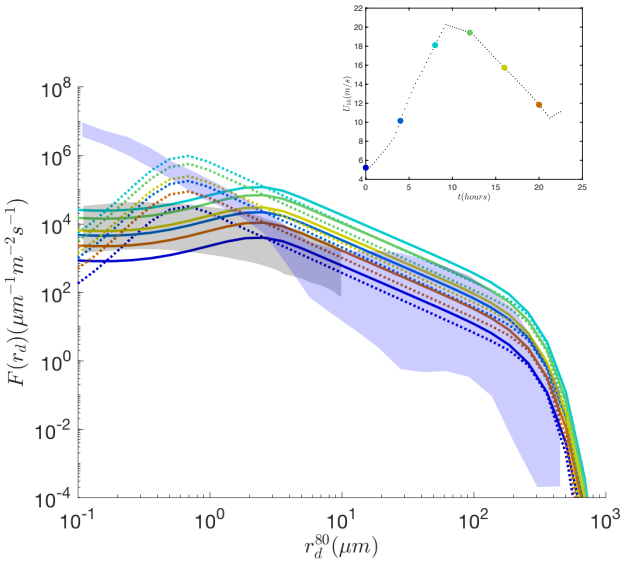

Figure 8

Sea spray generation function (SSGF) (eq. 29) during one storm in the Southern Ocean. Solid lines indicate the jet drop production function, assuming the smallest bubble bursting is 50μm. Dotted lines indicate the film drop production function, with the peak of drop produced being assumed to be 0.5μm. Jet drops dominates above 2μm in this representation. Radius is drop size at equilibrium at 80% relative humidity, $r_d^{80} = 0.5 r_d$. Colors indicate different times, with the corresponding wind speed shown in inset, increasing from 5 m/s to 20 m/s over 10 hours, and then setting down, with more drops ejected during the storm intensification, corresponding to more intense breaking events. Light blue area indicate typical SSGF summarized by Veron (2015) at 15m/s and light grey indicates typical SSGF summarized by Lewis & Schwartz (2004) at 8 m/s. The sea-state dependent formulation falls within the uncertainties of previous empirical data, and rationalize some of the variability previously reported.

5.3. Integration over breaking statistics and sea-state dependent sea spray source function

Finally, we use the air flux of bubbles under breaking waves, defined as the number per unit ocean surface area per unit time, $Q(R_b)$, related to the air volume flux V_A (eq. 14 and 20 see Deike et al. (2017a); Deike & Melville (2018)), to propose a sea-state dependent sea-spray source function resulting from bubble bursting.

We write $F_d(r_d)$ the sea spray generation function, resulting from one of the two bursting mechanism, as the integration of the bubble flux distribution $Q(R_b)$ with the bursting production function, or distribution of drops produced by bubbles of size between R_b and $R_b + dR_b$, $G(r_d, R_b)dR_b = \frac{n(R_b)}{\langle r_d \rangle} p(r_d/\langle r_d \rangle)dR_b$. The function $G(r_d, R_b)$ translates a bubble distribution (in the water bulk) into a drop distribution (in the air). For now, we assume that all bubbles within the bounds considered will burst in a way comparable to the single bubble bursting studies. This yields a sea-spray source function F_d, defined as number of drops per unit surface ocean area, per unit time (same units as $Q(R_b)$), physically consistent with the existing literature on sea spray generation function,

$$F_d(r_d) = \int\left(Q(R_b)\frac{n(R_b)}{\langle r_d\rangle}p\left(\frac{r_d}{\langle r_d\rangle}\right)\right)dR_b \tag{28}$$

$$= \int\int\left(\frac{B}{2\pi}\frac{s(k)^{3/2}c^3}{g}\Lambda(c)dc\frac{N(R_b)n(R_b)}{\langle r_d\rangle}p\left(\frac{r_d}{\langle r_d\rangle}\right)\right)dR_b \tag{29}$$

This naturally considers the sea-state effects through the $\Lambda(c)$ distribution, controlling the number flux of bubbles $Q(R_b)$, while physico-chemical control on the droplet production are included within $G(r_d, R_b)$, $n(R_b)$, $\langle r_d\rangle(R_b)$ and $p(r_d/\langle r_d\rangle)$. The sea-spray generation function for film an jet drops (between their drop size bounds) follows

$$F_d(r_d)^{film} \propto r_d^{-7/4}V_A; \text{ and } F_d(r_d)^{jet} \propto r_d^{-5/3}V_A \tag{30}$$

Figure 8 shows the result of integration of Eq. 29, for a 24 hour storm in the Southern Ocean, modeled using WW3 (same conditions as for the gas transfer velocity in §4). We use reasonable guesses for the bounds of production of film drop with bubbles from 1mm to 10mm, and minimal film thickness of 0.1μm, leading to a drop size distribution peaking at 0.5μm, and up to 400μm. Jet drops are considered for bubbles from 50μm to 2mm, with a peak at 2μm and up to 800μm. The prefactor for the drop productions are those suggested in figure 6 and 7 following Lhuissier & Villermaux (2012); Berny et al. (2021). In this representation, jet drops dominate the production above 2μm. This highlights the importance of understanding the bounds of production for jet and film drops, as both mechanisms are shown to produce drops in comparable ranges, as well as refining the constraints on the number of drops being produced, especially for film drop, as it might shift the range of sizes where one mechanism dominates over the other.

The resulting sea spray source function is fully compatible with typical functions used in the literature and reviewed in Lewis & Schwartz (2004); Veron (2015); de Leeuw et al. (2011) which indicates the high potential of this approach; which incorporate physical dependency on sea-state, as well as temperature conditions. The drop production is higher during the storm intensification than during the set-down, for the same wind speed, which rationalize some of the natural variability reported in existing field measurements.

5.4. Surfactants and the physico-chemistry of the interface

We have discussed jet and film drops produced by bursting, and considered the role of viscosity, density and surface tension in setting the film thickness and cavity collapse, controlling the film and jet drops properties. The ocean surface is partly covered by a biofilm, which can be modeled as surfactant (Wurl et al. 2011), with surface-active materials known to modify the static and dynamic behaviors of bubbles, including coalescence, life-time and bursting, for contaminations at which the static tension is still close to its clean value (Langevin & Rio 2015; Poulain et al. 2018; Shaw & Deike 2021; Neel & Deike 2021).

Neel & Deike (2021) considered a nearly monodisperse assembly of millimetric air bubbles produced identically in the bulk for a wide range of surface contamination, and showed two asymptotic regimes: for low contamination, bubbles are short-lived and coalesce systematically, exhibiting bubbles aggregating up to a hundred times their initial volume, and leading to broad distributions distinct from monodisperse bubbles. At high contamination, bubbles have an extended life-time and coalescence is prevented, so that the surface bubbles distribution tends towards the bulk bubbles distribution. The ocean-water condition

are expected to be in an intermediate regime (Neel & Deike 2021). This implies that the knowledge of the *bulk* bubbles distribution might not be enough to predict the *surface* bubbles distribution, introducing a *bulk-surface transfer function* which depend on the bubble life-time and merging capability, itself a function of the water contamination, temperature and humidity conditions. Such transfer function, once developed, could be integrated to the framework presented above, with the ability to modify the surface size distribution of bubbles bursting at the surface $Q(R_b)$, and associated bounds of drop size and production efficiency.

Multiple experiments have attempted to describe the role of the physico-chemical parameters on droplets and aerosols production by bubble bursting. There exist large variations in protocols and results sometimes contradicting each other Frossard et al. (2019); Modini et al. (2013); Prather et al. (2013); Quinn et al. (2015); Bertram et al. (2018) on whether enrichment by biological activity, and the presence of surfactant might increase or decrease the sea spray aerosol production. The composition of the sea-surface microlayer has been shown to play a major role in the later composition of the aerosols, together with the spray production mechanisms (Cochran et al. 2017; Wang et al. 2017; Bertram et al. 2018). Combining the fluid mechanics of jet and film drop production with the associated chemical composition of the water droplet and final solid sea spray aerosols remains to be proposed.

SUMMARY POINTS

1. Canonical studies of breaking waves, bubble dynamics in turbulence and bubble bursting provide detailed descriptions of the local air-sea mass exchange.
2. Using a statistical representation of breaking waves and the resulting entrained air bubbles lead to a multi-scale formulation of air-sea fluxes controlled by breaking waves, naturally encompassing sea-state effects.
3. Application to propose a generic sea-state dependent bubble mediated gas transfer velocity (for various species), which collapse field data by accounting for wave effects, and provide a modeling path to account for sea-state variability.
4. Application to propose a sea-state dependent sea spray generation function due to bubble bursting, for film and jet drops, with natural temperature dependencies.

FUTURE ISSUES

1. The similarity hypothesis of breaking dynamics, air entrainment and bubble statistics should be tested in the field through detailed near surface measurements of the two-phase turbulent process.
2. Systematic field observations of breaking statistics, jointly with gas transfer and near surface spray production is necessary to further validate the proposed models.
3. The role of surface collective bubble dynamic on jet and film drop production needs to be evaluated, together with the role of contamination and its influence on the jet and film drop production efficiency, and range of sizes produced.
4. The links between the physical mechanisms of spray formation and the aerosol chemical composition, which starts to be better understood need to be further developed and integrated in mechanistic sea spray aerosol generation function.

5. The importance of sea-state dependent parameterization of gas exchange and sea spray production on large scale ocean, atmospheric and climate dynamics needs to be assessed by performing coupled modeling.
6. The representation of breaking waves and associated gas and spray fluxes at very high wind speed (above 25 m/s), for which the definition of individual events will cease to be valid, remains an open challenge.

DISCLOSURE STATEMENT

The authors are not aware of any affiliations, memberships, funding, or financial holdings that might be perceived as affecting the objectivity of this review.

ACKNOWLEDGMENTS

I am grateful to my scientific mentor Ken Melville for introducing me to the field of air-sea interactions, as well as Stephane Popinet for his continuous support and our common work on modeling interfacial flows. I thank Peter Sutherland, Leonel Romero, Luc Lenain and Henri Lhuissier for providing their published figures and data, and Brandon Reichl for providing WAVEWATCHIII outputs. This work has been supported by NSF Grant 1849762, NSF CAREER award 1844932 to L.D. and the Cooperative Institute for Earth System modeling between Princeton and the Geophysical Fluid Dynamics Laboratory (GFDL) NOAA.

LITERATURE CITED

Aliseda A, Lasheras J. 2011. Preferential concentration and rise velocity reduction of bubbles immersed in a homogeneous and isotropic turbulent flow. *Physics of Fluids* 23:093301

Ardhuin F, Rogers E, Babanin AV, Filipot JF, Magne R, et al. 2010. Semiempirical dissipation source functions for ocean waves. part i: Definition, calibration, and validation. *Journal of Physical Oceanography* 40:1917–1941

Atamanchuk D, Koelling J, Send U, Wallace D. 2020. Rapid transfer of oxygen to the deep ocean mediated by bubbles. *Nature Geoscience* 13:232–237

Banner M, Peirson WL. 2007. Wave breaking onset and strength for two-dimensional deep-water wave groups. *J. Fluid Mech.* 585:93–115

Banner M, Zappa C, Gemmrich J. 2014. A note on the phillips spectral framework for ocean whitecaps. *Journal of Physical Oceanography* 44:1727–1734

Bell TG, Landwehr S, Miller SD, Bruyn WJ, Callaghan AH, et al. 2017. Estimation of bubble-mediated air–sea gas exchange from concurrent DMS and CO_2 transfer velocities at intermediate–high wind speeds. *Atmospheric Chemistry and Physics* 17:9019–9033

Berny A, Deike L, Séon T, Popinet S. 2020. Role of all jet drops in mass transfer from bursting bubbles. *Physical Review Fluids* 5:033605

Berny A, Seon T, Popinet S, Deike L. 2021. Statistics of jet drop production. *GRL* Submitted

Bertram TH, Cochran RE, Grassian VH, Stone EA. 2018. Sea spray aerosol chemical composition: elemental and molecular mimics for laboratory studies of heterogeneous and multiphase reactions. *Chemical Society Reviews* 47:2374–2400

Blanchard DC. 1963. The electrification of the atmosphere by particles from bubbles in the sea. *Progress In Oceanography* 1:73 – 112, IN7, 113–202

Blanchard DC, Syzdek LD. 1988. Film drop production as a function of bubble size. *Journal of Geophysical Research: Oceans* 93:3649–3654

Blanco-Rodríguez FJ, Gordillo J. 2020. On the sea spray aerosol originated from bubble bursting jets. *Journal of Fluid Mechanics* 886

Blenkinsopp CE, Chaplin JR. 2010. Bubble size measurements in breaking waves using optical fiber phase detection probes. *Oceanic Engineering, IEEE Journal of* 35:388–401

Bowyer PA. 2001. Video measurements of near-surface bubble spectra. *Journal of Geophysical Research: Oceans* 106:14179–14190

Brasz CF, Bartlett CT, Walls PLL, Flynn EG, Yu YE, Bird JC. 2018. Minimum size for the top jet drop from a bursting bubble. *Phys. Rev. Fluids* 3

Brumer S, Zappa C, Blomquist B, Fairall C, Cifuentes-Lorenzen A, et al. 2017a. Wave-related reynolds number parameterizations of CO_2 and DMS transfer velocities. *Geophysical Research Letters* 44:9865–9875

Brumer SE, Zappa CJ, Brooks IM, Tamura H, Brown SM, et al. 2017b. Whitecap coverage dependence on wind and wave statistics as observed during so gasex and hiwings. *Journal of Physical Oceanography* 47:2211–2235

Callaghan A, de Leeuw G, Cohen L, O'Dowd CD. 2008. Relationship of oceanic whitecap coverage to wind speed and wind history. *Geophysical Research Letters* 35

Callaghan A, Deane G, Stokes M. 2017. On the imprint of surfactant-driven stabilization of laboratory breaking wave foam with comparison to oceanic whitecaps. *Journal of Geophysical Research: Oceans*

Callaghan AH, Deane GB, Stokes DM. 2013. Two regimes of laboratory whitecap foam decay: bubble-plume controlled and surfactant stabilized. *J. Phys. Oceanography*

Cavaleri L, Fox-Kemper B, Hemer M. 2012. Wind waves in the coupled climate system. *Bulletin of the American Meteorological Society* 93:1651–1661

Chan WHR, Johnson PL, Moin P, Urzay J. 2020. The turbulent bubble break-up cascade. part 2. numerical simulations of breaking waves. *arXiv preprint arXiv:2009.04804*

Chen G, Kharif C, Zaleski S, Li J. 1999. Two dimensionnal navier stokes simulation of breaking waves. *Phys. Fluid* 11:121–133

Cipriano RJ, Blanchard DC. 1981. Bubble and aerosol spectra produced by a laboratory breaking wave. *Journal of Geophysical Research: Oceans* 86:8085–8092

Cochran RE, Ryder OS, Grassian VH, Prather KA. 2017. Sea spray aerosol: The chemical link between the oceans, atmosphere, and climate. *Accounts of chemical research* 50:599–604

de Leeuw G, Andreas EL, Anguelova MD, Fairall CW, Lewis ER, et al. 2011. Production flux of sea spray aerosol. *Rev. Geophys.* 49

De Vita F, Verzicco R, Iafrati A. 2018. Breaking of modulated wave groups: kinematics and energy dissipation processes. *Journal of fluid mechanics* 855:267–298

Deane GB, Stokes MD. 2002. Scale dependence of bubble creation mechanisms in breaking waves. *Nature* 418:839–844

Deike L, Ghabache E, Liger-Belair G, Das AK, Zaleski S, et al. 2018. The dynamics of jets produced by bursting bubbles. *Phys. Rev. Fluids* 3

Deike L, Lenain L, Melville WK. 2017a. Air entrainment by breaking waves. *Geophysical Research Letters* 44:3779–3787

Deike L, Melville W, Popinet S. 2016. Air entrainment and bubble statistics in breaking waves. *J. Fluid Mech.* 801:91–129

Deike L, Melville WK. 2018. Gas transfer by breaking waves. *Geophysical Research Letters* 45:10–482

Deike L, Pizzo N, Melville W. 2017b. Lagrangian mass transport by surface breaking waves. *J. Fluid Mech.* 829:364391

Deike L, Popinet S, Melville W. 2015. Capillary effects on wave breaking. *J. Fluid Mech.* 769:541–569

Derakhti M, Kirby JT. 2016. Breaking-onset, energy and momentum flux in unsteady focused wave

packets. *J. Fluid Mech.* 790:553–581

Derakhti M, Kirby JT, Banner ML, Grilli ST, Thomson J. 2020. A unified breaking onset criterion for surface gravity water waves in arbitrary depth. *Journal of Geophysical Research: Oceans* :e2019JC015886

Dommermuth DG, Yue DK, Lin W, Rapp R, Chan E, Melville W. 1988. Deep-water plunging breakers: a comparison between potential theory and experiments. *Journal of Fluid Mechanics* 189:423–442

Drazen DA, Melville WK, Lenain L. 2008. Inertial scaling of dissipation in unsteady breaking waves. *J. Fluid Mech.* 611:307–332

Duchemin L, Popinet S, Josserand C, Zaleski S. 2002. Jet formation in bubbles bursting at a free surface. *Phys. Fluids* 14:3000–3008

Duncan J. 1981. An experimental investigation of breaking waves produced by a towed hydrofoil. *Proceedings of the Royal Society of London. A. Mathematical and Physical Sciences* 377:331–348

Duncan JH. 2001. Spilling breakers. *Annual review of fluid mechanics* 33:519–547

Edson J, Fairall C, Bariteau L, Zappa CJ, Cifuentes-Lorenzen A, et al. 2011. Direct covariance measurement of CO_2 gas transfer velocity during the 2008 southern ocean gas exchange experiment: Wind speed dependency. *Journal of Geophysical Research: Oceans* 116

Eggers J, Villermaux E. 2008. Physics of liquid jets. *Reports on progress in physics* 71:036601

Emerson S, Bushinsky S. 2016. The role of bubbles during air-sea gas exchange. *Journal of Geophysical Research: Oceans* 121:4360–4376

Emerson S, Yang B, White M, Cronin M. 2019. Air-sea gas transfer: Determining bubble fluxes with in situ n2 observations. *Journal of Geophysical Research: Oceans* 124:2716–2727

Erinin MA, Wang SD, Liu R, Towle D, Liu X, Duncan JH. 2019. Spray generation by a plunging breaker. *Geophysical Research Letters* 46:8244–8251

Esters L, Landwehr S, Sutherland G, Bell TG, Christensen KH, et al. 2017. Parameterizing air-sea gas transfer velocity with dissipation. *Journal of Geophysical Research: Oceans* 122:3041–3056

Fairall C, Bradley EF, Hare J, Grachev A, Edson J. 2003. Bulk parameterization of air–sea fluxes: Updates and verification for the coare algorithm. *Journal of climate* 16:571–591

Farsoiya PK, Popinet S, Deike L. 2021. Bubble-mediated gas transfer in turbulence. *Journal of Fluid Mechanics* In Review

Fitzgerald JW. 1975. Approximation formulas for the equilibrium size of an aerosol particle as a function of its dry size and composition and the ambient relative humidity. *Journal of Applied Meteorology and Climatology* 14:1044–1049

Friedlingstein P, O'Sullivan M, Jones MW, Andrew RM, Hauck J, et al. 2020. Global carbon budget 2020. *Earth System Science Data* 12:3269–3340

Frossard AA, Long MS, Keene WC, Duplessis P, Kinsey JD, et al. 2019. Marine aerosol production via detrainment of bubble plumes generated in natural seawater with a forced-air venturi. *Journal of Geophysical Research: Atmospheres* 124:10931–10950

Gañán-Calvo AM. 2017. Revision of bubble bursting: universal scaling laws of top jet drop size and speed. *Physical review letters* 119:204502

Garbe CS, Rutgersson A, Boutin J, de Leeuw G, Delille B, et al. 2014. Transfer across the air-sea interface. Berlin, Heidelberg: Springer Berlin Heidelberg, 55–112

Garrett C, Li M, Farmer D. 2000. The connection between bubble size spectra and energy dissipation rates in the upper ocean. *J. Phys. Oceanogr.* 30:2163–2171

Gemmrich JR, Banner ML, Garrett C. 2008. Spectrally resolved energy dissipation rate and momentum flux of breaking waves. *J. Phys. Oceanography* 38:1296–1312

Ghabache E, Antkowiak A, Josserand C, Séon T. 2014. On the physics of fizziness: How bubble bursting controls droplets ejection. *Physics of Fluids (1994-present)* 26:–

Ghabache E, Séon T. 2016. Size of the top jet drop produced by bubble bursting. *Phys. Rev. Fluids* 1

Gordillo J, Rodríguez-Rodríguez J. 2019. Capillary waves control the ejection of bubble bursting

jets. *Journal of Fluid Mechanics* 867:556–571

Grare L, Peirson WL, Branger H, Walker JW, Giovanangeli JP, Makin V. 2013. Growth and dissipation of wind-forced, deep-water waves. *J. Fluid Mech.* 722:5–50

Hasselmann K. 1962. On the non-linear energy transfer in a gravity-wave spectrum. *J. Fluid Mech* 12:481–500

Hasselmann K, Barnett TP, Bouws E, Carlson H, Cartwright DE, et al. 1973. Measurements of wind-wave growth and swell decay during the joint north sea wave project (jonswap). *Ergänzungsheft 8-12*

Hinze JO. 1955. Fundamentals of the hydrodynamic mechanism of splitting in dispersion processes. *AIChE Journal* 1:289–295

Ho DT, Law CS, Smith MJ, Schlosser P, Harvey M, Hill P. 2006. Measurements of air-sea gas exchange at high wind speeds in the southern ocean: Implications for global parameterizations. *Geophysical Research Letters* 33

Ho DT, Wanninkhof R, Schlosser P, Ullman DS, Hebert D, Sullivan KF. 2011. Toward a universal relationship between wind speed and gas exchange: Gas transfer velocities measured with 3he/sf6 during the southern ocean gas exchange experiment. *Journal of Geophysical Research: Oceans* 116

Iafrati A. 2009. Numerical study of the effects of the breaking intensity on wave breaking flows. *Journal of Fluid Mechanics* 622:371

Keeling RF. 1993. On the role of large bubbles in air-sea gas exchange and supersaturation in the ocean. *Journal of Marine Research* 51:237–271

Kleiss JM, Melville WK. 2010. Observations of wave breaking kinematics in fetch-limited seas. *J. Phys. Oceanogr.* 40:2575–2604

Komen GJ, Cavaleri L, Donelan M, Hasselmann K, Hasselmann S, Janssen P. 1996. Dynamics and modelling of ocean waves

Lai CY, Eggers J, Deike L. 2018. Bubble bursting: Universal cavity and jet profiles. *Physical review letters* 121:144501

Lamarre E, Melville W. 1991. Air entrainment and dissipation in breaking waves. *Nature* 351:469–472

Langevin D, Rio E. 2015. Foams and Emulsions: Coalescence. In *Encyclopedia of Surface and Colloid Science*, ed. P Somasundaran. CRC Press, 3rd ed., 2837–2851

Leighton TG, Coles DG, Srokosz M, White PR, Woolf DK. 2018. Asymmetric transfer of co 2 across a broken sea surface. *Scientific reports* 8:1–9

Lenain L, Melville W. 2017a. Evidence of sea-state dependence of aerosol concentration in the marine atmospheric boundary layer. *J. Phys. Oceanography* 47:6984

Lenain L, Melville WK. 2017b. Measurements of the directional spectrum across the equilibrium saturation ranges of wind-generated surface waves. *J. Phys. Oceanogr.* 47:2123–2138

Lenain L, Pizzo N. 2020. The contribution of high-frequency wind-generated surface waves to the stokes drift. *Journal of Physical Oceanography* 50:3455–3465

Levich VG. 1962. Physicochemical hydrodynamics

Lewis ER, Schwartz SE. 2004. Sea salt aerosol production. mechanisms, methods, measurements, and models. Washington, DC,: American Geophysical Union, geophysical monograph 152. ed.

Lhuissier H, Villermaux E. 2012. Bursting bubble aerosols. *J. Fluid Mech.* 696:5–44

Liang J, McWilliams JC, Sullivan PP, Baschek B. 2011. Modeling bubbles and dissolved gases in the ocean. *J. Geophys. Res.* 116

Liang JH, Emerson SR, D'Asaro EA, McNeil CL, Harcourt RR, et al. 2017. On the role of sea-state in bubble-mediated air-sea gas flux during a winter storm. *Journal of Geophysical Research: Oceans* :n/a–n/a

Liang JH, McWilliams J, Sullivan P, Baschek B. 2012. Large eddy simulation of the bubbly ocean: New insights on subsurface bubble distribution and bubble-mediated gas transfer. *J. Geophys. Res.* 117

Loewen MR, O'Dor MA, Skafel MG. 1996. Bubbles entrained by mechanically generated breaking waves. *J. Geophys. Res.* 101:20759–20769

Longuet-Higgins MS. 1957. The statistical analysis of a random, moving surface. *Philosophical Transactions of the Royal Society of London. Series A, Mathematical and Physical Sciences* 249:321–387

Longuet-Higgins MS, Dommermuth DG. 1997. Crest instabilities of gravity waves. part 3. non linear development and breaking. *J. Fluid Mech.* 336:33–50

Lubin P, Glockner S. 2015. Numerical simulations of three-dimensional plunging breaking waves: generation and evolution of aerated vortex filaments. *J. Fluid Mech.* 767:364–393

Mårtensson E, Nilsson E, de Leeuw G, Cohen L, Hansson HC. 2003. Laboratory simulations and parameterization of the primary marine aerosol production. *Journal of Geophysical Research: Atmospheres* 108

Martinez-Bazan C, Montanes J, Lasheras J. 1999. On the breakup of an air bubble injected into a fully developed turbulent flow. part 1. breakup frequency. *J. Fluid Mech.* 401:157–182

Melville WK. 1982. The instability and breaking of deep-water waves. *J. Fluid Mech.* 115:165–185

Melville WK. 1996. The role of surface wave breaking in air-sea interaction. *Annu. Rev. Fluid Mech.* 28:279–321

Melville WK, Fedorov AV. 2015. The equilibrium dynamics and statistics of gravity-capillary waves. *J. Fluid Mech.* 767:449–466

Melville WK, Veron F, White CJ. 2002. The velocity field under breaking waves: coherent structure and turbulence. *J. Fluid. Mech.* 454

Miles JW. 1957. On the generation of surface waves by shear flows. *Journal of Fluid Mechanics* 3:185–204

Miller S, Marandino C, De Bruyn W, Saltzman E. 2009. Air-sea gas exchange of CO_2 and DMS in the north atlantic by eddy covariance. *Geophysical Research Letters* 36

Modini R, Russell L, Deane G, Stokes M. 2013. Effect of soluble surfactant on bubble persistence and bubble-produced aerosol particles. *Journal of Geophysical Research: Atmospheres* 118:1388–1400

Monahan EC, Muircheartaigh I. 1980. Optimal power-law description of oceanic whitecap coverage dependence on wind speed. *Journal of Physical Oceanography* 10:2094–2099

Mostert W, Popinet S, Deike L. 2021. High-resolution direct simulation of deep water breaking waves: transition to turbulence, bubbles and droplets production. *Submitted*

Mueller J, Veron F. 2009. A sea state-dependent spume generation function. *J. Phys. Oceanogr.* 39:2363–2372

Neel B, Deike L. 2021. Collective surface bubbles dynamics and bursting, and the role of surface contamination. *In Review*

Néel B, Villermaux E. 2018. The spontaneous puncture of thick liquid films. *Journal of Fluid Mechanics* 838:192

Ortiz-Suslow DG, Haus BK, Mehta S, Laxague NJ. 2016. Sea spray generation in very high winds. *Journal of the Atmospheric Sciences* 73:3975–3995

Perlin M, Choi W, Tian Z. 2013. Breaking waves in deep and intermediate waters. *Annual Review of Fluid Mechanics* 45:115–145

Perrard S, Rivière A, Mostert W, Deike L. 2021. Bubble deformation by a turbulent flow. *In Review, Journal of Fluid Mechanics* arXiv:2011.1054

Phillips O. 1985. Spectral and statistical properties of the equilibrium range in wind-generated gravity waves. *J. Fluid Mech.* 156:505–31

Pizzo N, Deike L, Melville W. 2016. Current generation by deep-water breaking waves. *J. Fluid Mech.* 803:275–291

Pizzo N, Melville WK. 2013. Vortex generation by deep-water breaking waves. *J. Fluid Mech.* 734:198–218

Pizzo N, Melville WK, Deike L. 2019. Lagrangian transport by nonbreaking and breaking deep-water waves at the ocean surface. *Journal of Physical Oceanography* 49:983–992

Plant WJ. 1982. A relationship between wind stress and wave slope. *Journal of Geophysical Research: Oceans* 87:1961–1967

Poorte RE, Biesheuvel A. 2002. Experiments on the motion of gas bubbles in turbulence generated by an active grid. *Journal of Fluid Mechanics* 461:127–154

Poulain S, Villermaux E, Bourouiba L. 2018. Ageing and burst of surface bubbles. *Journal of Fluid Mechanics* 851:636–671

Prather KA, Bertram TH, Grassian VH, Deane GB, Stokes MD, et al. 2013. Bringing the ocean into the laboratory to probe the chemical complexity of sea spray aerosol. *Proceedings of the National Academy of Sciences* 110:7550–7555

Quinn PK, Collins DB, Grassian VH, Prather KA, Bates TS. 2015. Chemistry and related properties of freshly emitted sea spray aerosol. *Chemical reviews* 115:4383–4399

Rapp R, Melville W. 1990. Laboratory measurements of deep-water breaking waves. *Philosophical Transactions of the Royal Society of London. Series A, Mathematical and Physical Sciences* 331:735–800

Reichl BG, Deike L. 2020. Contribution of sea-state dependent bubbles to air-sea carbon dioxide fluxes. *Geophysical Research Letters* :e2020GL087267

Resch F, Afeti G. 1991. Film drop distributions from bubbles bursting in seawater. *Journal of Geophysical Research: Oceans* 96:10681–10688

Richter DH, Dempsey AE, Sullivan PP. 2019. Turbulent transport of spray droplets in the vicinity of moving surface waves. *Journal of Physical Oceanography* 49:1789–1807

Rivière A, Mostert W, Perrard S, Deike L. 2021. Sub-hinze scale bubble production in turbulent bubble break-up. *Journal of Fluid Mechanics* In Review

Rojas G, Loewen M. 2007. Fiber-optic probe measurements of void fraction and bubble size distributions beneath breaking waves. *Experiments in Fluids* 43:895–906

Romero L. 2019. Distribution of surface wave breaking fronts. *Geophysical Research Letters* 46:10463–10474

Romero L, Melville WK. 2010. Airborne observations of fetch-limited waves in the gulf of tehuantepec. *J. Phys. Oceanography* 40:441–465

Romero L, Melville WK. 2011. Spatial statistics of the sea surface in fetch-limited conditions. *Journal of physical oceanography* 41:1821–1841

Romero L, Melville WK, Kleiss JM. 2012. Spectral energy dissipation due to surface wave breaking. *J. Phys. Oceanogr* 42:1421–1441

Ruth DJ, Vernet M, Perrard S, Deike L. 2021. Bubble rise velocity in turbulence. *Journal of Fluid Mechanics* In review

Saket A, Peirson WL, Banner ML, Barthelemy X, Allis MJ. 2017. On the threshold for wave breaking of two-dimensional deep water wave groups in the absence and presence of wind. *Journal of Fluid Mechanics* 811:642

Salibindla AK, Masuk AUM, Tan S, Ni R. 2020. Lift and drag coefficients of deformable bubbles in intense turbulence determined from bubble rise velocity. *Journal of Fluid Mechanics*

Schwendeman M, Thomson J. 2015. Observations of whitecap coverage and the relation to wind stress, wave slope, and turbulent dissipation. *Journal of Geophysical Research: Oceans* 120:8346–8363

Schwendeman M, Thomson J, Gemmrich JR. 2014. Wave breaking dissipation in a young wind sea. *Journal of Physical Oceanography* 44:104–127

Sellegri K, O'Dowd C, Yoon Y, Jennings S, de Leeuw G. 2006. Surfactants and submicron sea spray generation. *Journal of Geophysical Research: Atmospheres* 111

Shaw D, Deike L. 2021. Surface bubble coalescence. *In press*

Soligo G, Roccon A, Soldati A. 2019. Breakage, coalescence and size distribution of surfactant-laden droplets in turbulent flow. *Journal of Fluid Mechanics* 881:244–282

Spiel DE. 1994. The number and size of jet drops produced by air bubbles bursting on a fresh water surface. *J. Geophys. Res.* 99:10289–10296

Spiel DE. 1997. More on the births of jet drops from bubbles bursting on seawater surfaces. *J. Geophys. Res.* 102:5815–5821

Stanley RH, Jenkins WJ, Lott III DE, Doney SC. 2009. Noble gas constraints on air-sea gas exchange and bubble fluxes. *Journal of Geophysical Research: Oceans* 114

Sullivan PP, McWilliams JC. 2010. Dynamics of winds and currents coupled to surface waves. *Annual Review of Fluid Mechanics* 42

Sutherland P, Melville WK. 2013. Field measurements and scaling of ocean surface wave-breaking statistics. *Geophysical Research Letters* 40:3074–3079

Sutherland P, Melville WK. 2015. Field measurements of surface and near-surface turbulence in the presence of breaking waves. *Journal of Physical Oceanography* 45:943–965

Thomson J, Gemmrich JR, Jessup AT. 2009. Energy dissipation and the spectral distribution of whitecaps. *Geophysical Research Letters* 36

Tian Z, Perlin M, Choi W. 2010. Energy dissipation in two-dimensional unsteady plunging breakers and an eddy viscosity model. *J. Fluid Mech.* 655:217–257

Toba Y. 1972. Local balance in the air-sea boundary processes. *Journal of Oceanography* 28:109–120

Troitskaya Y, Kandaurov A, Ermakova O, Kozlov D, Sergeev D, Zilitinkevich S. 2018. The bag breakup spume droplet generation mechanism at high winds. part i: Spray generation function. *Journal of physical oceanography* 48:2167–2188

Tsai Wt, Hung L. 2007. Three-dimensionnal modeling of small-scale processes in the upper boundary layer bounded by a dynamic ocean surface. *Journal of Geophysical Research* 112:C02019

Veron F. 2015. Ocean spray. *Ann. Rev. Fluid Mech.* 47:507–538

Veron F, Hopkins C, Harrison E, Mueller J. 2012. Sea spray spume droplet production in high wind speeds. *Geophysical Research Letters* 39

Villermaux E. 2020. Fragmentation versus cohesion. *Journal of Fluid Mechanics* 898

Walls P, Henaux L, Bird JC. 2015. Jet drops from bursting bubbles: How gravity and viscosity couple to inhibit droplet production. *Phys. Rev, E* 92:021002

Wang X, Deane GB, Moore KA, Ryder OS, Stokes MD, et al. 2017. The role of jet and film drops in controlling the mixing state of submicron sea spray aerosol particles. *Proceedings of the National Academy of Sciences* :201702420

Wang Z, Yang J, Stern F. 2016. High-fidelity simulations of bubble, droplet and spray formation in breaking waves. *Journal of Fluid Mechanics* 792:307–327

Wanninkhof R. 2014. Relationship between wind speed and gas exchange over the ocean revisited. *Limnology and Oceanography: Methods* 12:351–362

Wanninkhof R, Asher W, Ho D, Sweeney C, McGillis W. 2009. Advances in quantifying air-sea gas exchange and environmental forcing. *Annual Reviews of Marine Science*

Woolf DK. 2005. Parametrization of gas transfer velocities and sea-state-dependent wave breaking. *Tellus B* 57:87–94

Woolf DK, Shutler JD, Goddijn-Murphy L, Watson A, Chapron B, et al. 2019. Key uncertainties in the recent air-sea flux of co2. *Global Biogeochemical Cycles*

Woolf DK, Thorpe S. 1991. Bubbles and the air-sea exchange of gases in near-saturation conditions. *Journal of Marine Research* 49:435–466

Wurl O, Wurl E, Miller L, Johnson K, Vagle S. 2011. Formation and global distribution of sea-surface microlayers. *Biogeosciences* 8:121–135

Yang Z, Deng BQ, Shen L. 2018. Direct numerical simulation of wind turbulence over breaking waves. *Journal of Fluid Mechanics* 850:120–155

Zakharov VE, Badulin SI, Hwang PA, Caulliez G. 2015. Universality of sea wave growth and its physical roots. *J. Fluid Mech.* 780:503–535

Zakharov VE, L'vov VS, Falkovich G. 2012. Kolmogorov spectra of turbulence i: Wave turbulence. Springer Science & Business Media

Zappa CJ, Asher WE, Jessup AT. 2001. Microscale wave breaking and air-water gas transfer. *Journal of Geophysical Research: Oceans* 106:9385–9391

Zappa CJ, Banner M, Schultz H, Gemmrich J, Morison R, et al. 2012. An overview of sea state conditions and air-sea fluxes during radyo. *Journal of Geophysical Research: Oceans* 117